Region-specific and state-dependent astrocyte Ca^{2+} dynamics during the sleep-wake cycle in mice

Abbreviated title: Sleep/wake-dependent Ca^{2+} dynamics in astrocytes

Tomomi Tsunematsu[1, 2, 3, *], Shuzo Sakata[4], Tomomi Sanagi[2], Kenji F. Tanaka[5], and Ko Matsui[1]

[1]Super-network Brain Physiology, Graduate School of Life Sciences, Tohoku University, Sendai 980-8577, Japan

[2]Advanced Interdisciplinary Research Division, Frontier Research Institute for Interdisciplinary Sciences, Tohoku University, Sendai 980-8578, Japan

[3]Precursory Research for Embryonic Science and Technology, Japan Science and Technology Agency, Kawaguchi 332-0012, Japan

[4]Strathclyde Institute of Pharmacy and Biomedical Sciences, University of Strathclyde, Glasgow G4 0RE, UK

[5]Department of Neuropsychiatry, Keio University School of Medicine, Tokyo 160-8582, Japan

Address for correspondence:

Tomomi Tsunematsu, Ph.D.

E-mail: tsune@tohoku.ac.jp

Number of figures and tables: 5 figures and 2 tables

Number of Pages: 48

Number of words: Abstract (233), Significance statement (109), Introduction (639), and Discussion (1,500)

Conflict of interest:

The authors declare no competing financial interests associated with this study.

Acknowledgements:

This work was supported by PRESTO from the Japan Science and Technology Agency (JST) (grant no.: JPMJPR1887), and by Japan Society for the Promotion of Science (JSPS) KAKENHI (grant no.: 20H05047) to T.T., and a Grant-in-Aid for Scientific Research (B) (grant no.: 19H03338), Grant-in-Aid for Challenging Exploratory Research (grant no.: 18K19368), and a Toray Science Foundation grant to K.M. We thank A. Utsumi for assistance with the data analyses, Dr. S. Niwa for technical assistance, and Dr. Helena Akiko Popiel for English language editing of the manuscript.

Abstract

Neural activity is diverse, and varies depending on brain regions and sleep/wakefulness states. However, whether astrocyte activity differs between sleep/wakefulness states, and whether there are differences in astrocyte activity among brain regions remain poorly understood. Therefore, in this study, we recorded astrocyte intracellular calcium (Ca^{2+}) concentrations of mice during sleep/wakefulness states in the cortex, hippocampus, hypothalamus, cerebellum, and pons using fiber photometry. For this purpose, male transgenic mice expressing the genetically encoded ratiometric Ca^{2+} sensor YCnano50 specifically in their astrocytes were used. We demonstrated that Ca^{2+} levels in astrocytes substantially decrease during rapid eye movement (REM) sleep, and increase after the onset of wakefulness. In contrast, differences in Ca^{2+} levels during non-rapid eye movement (NREM) sleep were observed among the different brain regions, and no significant decrease was observed in the hypothalamus and pons. Further analyses focusing on the transition between sleep/wakefulness states and correlation analysis with the duration of REM sleep showed that Ca^{2+} dynamics differs among brain regions, suggesting the existence of several clusters; i.e., the first comprising the cortex and hippocampus, the second comprising the hypothalamus and pons, and the third comprising the cerebellum. Our study thus demonstrated that astrocyte Ca^{2+} levels change substantially according to sleep/wakefulness states. These changes were consistent in general unlike neural activity. However, we also clarified that Ca^{2+} dynamics varies depending on the brain region, implying that astrocytes may play various physiological roles in sleep.

63

Significance statement

Sleep is an instinctive behavior of many organisms. In the previous five decades, the mechanism of the neural circuits controlling sleep/wakefulness states and the neural activities associated with sleep/wakefulness states in various brain regions have been elucidated. However, whether astrocytes, which are a type of glial cell, change their activity during different sleep/wakefulness states was poorly understood. Here, we demonstrated that dynamic changes in astrocyte Ca^{2+} concentrations occur in the cortex, hippocampus, hypothalamus, cerebellum, and pons of mice during natural sleep. Further analyses demonstrated that Ca^{2+} dynamics slightly differ among different brain regions, implying that the physiological roles of astrocytes in sleep/wakefulness might vary depending on the brain region.

Introduction

Astrocytes, which are the main subtype of glial cells, are essential for central nervous system development and function. Many previous studies have clarified that astrocytes have housekeeping roles in brain function, contributing to ion and neurotransmitter homeostasis, formation and maintenance of the blood-brain barrier (Sofroniew and Vinters, 2010; Bojarskaite et al., 2020), regulation of blood flow, metabolic support for neurons (Magistretti and Allaman, 2018), neurotransmitter recycling (Sofroniew and Vinters, 2010), and regulation of synaptogenesis and synaptic transmission (Allen, 2014; Allen and Eroglu, 2017). All of these physiological functions of astrocytes are strongly associated with the dynamics of their intracellular calcium (Ca^{2+}) concentration. Intrinsic signals, including those involving neurotransmitters, protons, cannabinoids, polyphosphate, and endothelin result in increases in astrocyte Ca^{2+} concentrations (Gourine et al., 2010; Navarrete and Araque, 2010; Filosa et al., 2012; Min and Nevian, 2012; Holmstrom et al., 2013). In turn, the activated astrocytes release neuroactive substances called gliotransmitters, which activate neurons and vascular smooth muscle (Sasaki et al., 2012; Araque et al., 2014; Beppu et al., 2014; Savtchouk and Volterra, 2018).

In addition, it has become clear that astrocytes are involved in the regulation and physiological functions of mammalian sleep (Frank, 2019). There is evidence that astrocytes regulate sleep pressure through soluble N-ethylmaleimide-sensitive factor attachment protein receptor (SNARE)-dependent adenosine release (Halassa et al., 2009; Florian et al., 2011). Astrocytes also promote the sleep-dependent clearance of

98 brain waste products, such as β-amyloid (Xie et al., 2013). The dysfunction of gap
99 junctions in astrocytes leads to the inability to transfer lactate to wake-promoting orexin
100 neurons in the lateral hypothalamic area, resulting in sleep disorders (Clasadonte et al.,
101 2017), whereas optogenetic stimulation of astrocytes in the hypothalamus increases
102 sleep (Pelluru et al., 2016). Furthermore, astrocytes also regulate cortical state
103 switching (Poskanzer and Yuste, 2016). These results strongly indicate that astrocytes
104 play a pivotal role in sleep as well as other brain functions.

105 However, astrocytic Ca^{2+} dynamics in natural sleep has been poorly
106 understood, although an imaging study demonstrated that general anesthesia disrupts
107 astrocyte Ca^{2+} signaling in mice (Thrane et al., 2012). Recent studies have recorded
108 astrocyte Ca^{2+} changes during sleep/wakefulness in mice, but to date, data have only
109 been reported for the cortex (Bojarskaite et al., 2020; Ingiosi et al., 2020). Accumulating
110 evidence has shown that astrocytes are heterogeneous with respect to their
111 transcriptomes and functions among various brain regions as well as among various
112 neuronal types (Chai et al., 2017; Morel et al., 2017; Zeisel et al., 2018; Batiuk et al.,
113 2020; Bayraktar et al., 2020; Lozzi et al., 2020). It is well known that neurons in various
114 brain regions, i.e., the hypothalamus, midbrain, and brainstem, control the
115 sleep/wakefulness state, as well as rapid eye movement (REM)/ non-REM (NREM)
116 sleep, via a flip-flop circuit. (Sakurai, 2007; Weber and Dan, 2016; Scammell et al.,
117 2017; Liu and Dan, 2019). However, little is known about how astrocyte Ca^{2+}
118 concentrations in brain regions other than the cortex change depending on the
119 sleep/wakefulness state, and whether there are dynamic differences in astrocyte Ca^{2+}

120 levels among the different brain regions. Therefore, in this study, we performed fiber
121 photometry recordings of astrocyte Ca^{2+} dynamics of the cerebellum, cortex,
122 hippocampus, hypothalamus, and pons of mice during the sleep-wake cycle. To
123 optically record astrocyte Ca^{2+} dynamics, we used megalencephalic
124 leukoencephalopathy with subcortical cysts 1 (*Mlc1*)-tetracygline transactivator (tTA);
125 TetO-YCnano50 bigenic mice (Horikawa et al., 2010; Tanaka et al., 2010; Tanaka et al.,
126 2012; Kanemaru et al., 2014) in which astrocytes specifically express YCnano50.
127 In this study, we demonstrated that astrocyte Ca^{2+} levels consistently
128 decrease during REM sleep, and immediately increase with the onset of wakefulness.
129 In contrast, differences in Ca^{2+} levels during NREM sleep were observed in various
130 brain regions. There was a significant decrease in Ca^{2+} levels in the cerebellum, cortex,
131 and hippocampus during NREM sleep, but no significant decrease was observed in the
132 hypothalamus and pons.
133

Materials and Methods

Animals

All experimental procedures involving animals were approved by the Animal Care and Use Committee of Tohoku University (approval no.: 2019LsA-018) and were conducted in accordance with the National Institute of Health guidelines. All efforts were made to minimize animal suffering and discomfort, and to reduce the number of animals used. *Mlc1*-tTA; TetO-YCnano50 mice, which were used to monitor the dynamics of intracellular calcium concentration in astrocytes, were produced by crossing *Mlc1*-tTA mice (Tanaka et al., 2010) with TetO-YCnano50 mice (Kanemaru et al., 2014). The following polymerase chain reaction (PCR) primer sets were used for mouse genotyping: MlcU-675 (5'- AAATTCAGGAAGCTGTGTGCCTGC-3') and mtTA24L (5'-CGGAGTTGATCACCTTGGACTTGT-3') for *Mlc1*-tTA mice; and tetO-up (5'-AGCAGAGCTCGTTTAGTGAACCGT-3') and intronlow (5'-AAGGCAGGATGATGACCAGGATGT-3') for TetO-YCnano50 mice. Mice were housed under a controlled 12 h/12 h light/dark cycle (light on hours: 8:30–20:30). Mice had *ad libitum* access to food and water. A total of 14 male mice (nine *Mlc1*-tTA; TetO-YCnano50 mice and five *Mlc1*-tTA mice as controls) were used in this study. The following number of mice were used for the recording of each brain area: cerebellum, three mice (five recordings); cortex, three mice (six recordings); hippocampus, one mouse (two recordings); hypothalamus, two mice (four recordings); pons, one mouse (two recordings). For the recording of control *Mlc1*-tTA mice, three mice were used

(eight recordings). For the freely moving recording, two *Mlc1*-tTA; TetO-YCnano50 mice and two *Mlc1*-tTA mice as controls were used.

Surgical procedures

Male *Mlc1*-tTA; TetO-YCnano50 bigenic mice and *Mlc1*-tTA monogenic mice (≥ 12 weeks of age) were used. Stereotaxic surgery was performed under anesthesia with pentobarbital (5 mg/kg, intraperitoneal injection as induction) and with isoflurane (1%–2% for maintenance) using a vaporizer for small animals (Bio Research Center) with the mice positioned in a stereotaxic frame (Narishige). Two bone screws were implanted on the skull as electrodes for cortical electroencephalograms (EEGs), and twisted wires (AS633, Cooner Wire) were inserted into the neck muscle as an electrode for electromyograms (EMGs). Another bone screw was implanted in the cerebellum as a ground. All electrodes were connected to a pin socket.

For fiber photometry experiments, a cannula (CF440-10, Thorlabs) with a glass optical fiber (φ 400 μm, 0.39 NA, Thorlabs) was implanted into the cortex (1.2 mm posterior, 3.1 mm lateral from bregma, 0.3 mm depth from the brain surface), hippocampus (1.7 mm posterior, 1.5 mm lateral from bregma, 1.3 mm depth from the brain surface), hypothalamus (1.8 mm posterior, 1.0 mm lateral from bregma, 4.5 mm depth from the brain surface), cerebellum (6.0 mm posterior, 1.0 mm lateral from bregma, and 0.5 mm depth from the brain surface), and pons (5.1 mm posterior, 1.2 mm lateral from bregma, and 3.5 mm depth from the brain surface). All electrodes and optical fiber cannulas were fixed to the skull with dental cement. To fixate the head of

177 mice, a stainless chamber frame (CF-10, Narishige) was also attached to the skull using
178 dental cement. After the surgery, the mice were left to recover for at least five days.
179 During the habituation period, mice were placed in a head-fix apparatus (MAG-1,
180 Narishige), by securing them by the stainless chamber frame and placing them into an
181 acrylic tube. This procedure was continued for at least five days, during which the
182 duration of head-fixation was gradually extended from ten to 120 min.
183
184 ***In vivo* fiber photometry experiments in the head-fixed condition**
185 To detect the dynamics of intracellular Ca^{2+} concentrations in astrocytes, a
186 fiber photometric system (Lucir) was used. A 420-nm violet light-emitting diode (LED)
187 (Doric) was used to obtain Ca^{2+}-dependent signals. Recording in the head-fixed
188 condition was performed for about five hrs a day. During recording, EEGs and EMGs
189 were recorded continuously, whereas excitation light (20 Hz, 5 msec in width) was
190 intermittently illuminated at random for 4 minutes each time. The input light was
191 reflected off a dichroic mirror (FF458-Di02, Semrock) coupled to an optical fiber. LED
192 power was 1.12 ± 0.18 mW/mm^2 at the fiber tip. Light emission of cyan and yellow
193 fluorescence from YCnano50 was collected via an optical fiber cannula, divided by a
194 dichroic mirror (FF509-FDi01, Semrock) into cyan (483/32 nm bandpass filter, Semrock)
195 and yellow (542/27 nm bandpass filter, Semrock), and detected by each photomultiplier
196 (Lucir). Excitation signals were generated by a pulse generator (AWG-50, Elmos) to
197 control the LEDs. Fluorescence data were acquired at a sampling rate of 1 kHz through
198 an analog-to-digital converter (Micro1401-3, Cambridge Electronic Design [CED]). At

199 the same time as the fluorescence recording, EEG and EMG signals were amplified
200 (DAM50, World Precision Instruments), filtered, and digitized at 1 kHz using an
201 analog-to-digital converter. EEG and EMG signals were high-pass- and
202 low-pass-filtered at 0.1 Hz and 300 Hz, respectively. Locomotion was induced by
203 pinching the tail with forceps. Data were recorded using Spike2 software (CED).
204
205 ***In vivo* sleep/wakefulness recording using freely moving mice**
206 For the analysis of freely moving mice, continuous EEG and EMG recordings
207 were performed through a slip ring (SPM-35-8P-03, HIKARI DENSHI), which was
208 designed so that the movement of the mice was unrestricted. EEG and EMG signals
209 were amplified (AB-610J, Nihon Koden), filtered (EEG, 0.75–20 Hz; EMG, 20–50 Hz),
210 digitized at a sampling rate of 128 Hz, and recorded using SleepSign software version 3
211 (Kissei Comtec).
212
213 **Histological analysis**
214 To confirm the position of the implanted optical fibers, mice were deeply
215 anesthetized with isoflurane and perfused sequentially with 20 mL of chilled saline and
216 20 mL of chilled 4% paraformaldehyde in phosphate buffer solution (Nacalai Tesque).
217 The brains were removed and immersed in the above fixation solution overnight at 4 °C,
218 and then immersed in 30% sucrose in phosphate-buffered saline (PBS) for at least two
219 days. The brains were quickly frozen in embedding solution (Sakura Finetek), and cut
220 into coronal sections using a cryostat (CM3050, Leica) at a thickness of 40 and 50 μm.

For immunostaining, to confirm the expression of YCnano50 in astrocytes, the brain sections of *Mlc1*-tTA; TetO-YCnano50 bigenic mice were incubated with mouse anti-S100β antiserum (1:1,000; S2532, Merck) or mouse anti-GFAP antiserum (1:2000; G3893, Merck) overnight at 4 °C. Then, the sections were incubated with CF594 donkey anti-mouse IgG (1:1,000; 20116-1, Nacalai Tesque) for 1 hr at room temperature, mounted onto APS-coated slides, coverslipped with 50% glycerol in PBS, and observed using a fluorescence microscope (BZ-9000, Keyence) or a confocal microscope (LSM800, Zeiss).

Data analysis

Sleep scoring

Polysomnographic recordings were automatically scored offline, with each epoch scored as wakefulness, NREM sleep, or REM sleep by SleepSign (KISSEI COMTEC), in 4-sec epochs, according to standard criteria (Radulovacki et al., 1984; Tobler et al., 1997). All vigilance state classifications assigned by SleepSign were confirmed visually. The same individual, blinded to mouse genotype and experimental condition, scored all EEG/EMG recordings. Spectral analysis of the EEGs was performed by fast Fourier transform, which yielded a power spectral profile with a 1-Hz resolution divided into delta (1–5 Hz), theta (6–10 Hz), alpha (10–13 Hz), beta (13–25 Hz), and gamma (30–50 Hz) waves. To quantify EMG amplitude, the root-mean-square (rms) was calculated.

Fiber photometry signal processing

In Figures 1, 2, 3, and 4, axoGraph was used to calculate yellow fluorescence protein (YFP) to cyan fluorescence protein (CFP) (Y/C) ratios. The average value of the YFP intensity and CFP intensity for each light illumination (5 msec) was calculated, and then the Y/C ratio was calculated. For the comparison of Y/C ratios during the sleep/wakefulness states, the Y/C ratio of each episode was normalized with the average value during wakefulness set as 1. For sleep/wakefulness state transition analyses, four consecutive epochs (16 sec) of one state followed immediately by eight consecutive epochs (32 sec) of a distinct state were used. To assess correlations between Y/C ratio and EEG/EMG power (Figs. 2 and 4), spectral densities of EEG signals in every 1-sec window were estimated at delta (1-5 Hz), theta (6-10 Hz), alpha (13-25 Hz), beta (13-25 Hz), and gamma (30-50 Hz) bands using the multitaper method (http://chronux.org/). EMG power was calculated as the common logarithm of a root-mean-square value in every 1-sec window. The mean of Y/C ratio in the corresponding 1-sec window was also calculated. Pearson's correlation coefficient was computed based on z-scored values in each state.

In Figure 5, all data analyses were performed by custom written MATLAB software (MathWorks). To compute normalized Y/C ratios during the time-normalized episodes, Y/C ratios were first normalized by the mean Y/C ratio during wakefulness. To obtain the time-normalized Ca^{2+} dynamics, each episode was segmented into 5 bins and the mean Y/C ratio was computed for each bin. Episodes were classified based on vigilance states before and after the episode.

265

266 **Decoding**

267 To decode sleep/wakefulness states based on Ca^{2+} signals, the same
268 approach as described previously was used (Tsunematsu et al., 2020). Briefly, the
269 mean Y/C ratio was computed in each corresponding window (4 sec). After training a
270 linear classifier, classification performance was calculated with 4-fold cross validation.

271

272 **Experimental design and statistical analysis**

273 Data are presented as the mean ± SEM unless otherwise stated. Statistical
274 analyses were performed using MATLAB. Multiple group comparisons were performed
275 by one-way analysis of variance (ANOVA) in samples with a Gaussian distribution, and
276 by the Kruskal-Wallis test in samples with a non-Gaussian distribution, with the *post-hoc*
277 Bonferroni test. In Figure 5B, one-way ANOVA with the *post-hoc* Tukey's honest
278 significance difference (HSD) test was performed. *P*-values of less than 0.05 were
279 considered to indicate a statistically significant difference between groups. To calculate
280 effect size, power analyses were performed using G*Power 3.1 (Faul et al., 2007).

281

Results

Fiber photometry recording of Ca^{2+} signals in cerebellar astrocytes

To elucidate the dynamics of intracellular Ca^{2+} concentration in astrocytes during sleep/wakefulness states, we used *Mlc1*-tTA; TetO-YCnano50 bigenic mice. Mlc1 is an astrocyte-specific protein with unknown function, which is highly expressed in perivascular astrocyte end-feet and astrocyte-astrocyte contacts (Boor et al., 2005; Teijido et al., 2007). We first focused on cerebellar astrocytes, and investigated the Ca^{2+} changes. It has been reported that the activity of Bergmann glial cells, a specific type of radial astrocyte in the cerebellum, is inhibited in the anesthetized state compared with in the awake state (Hoogland et al., 2009; Nimmerjahn et al., 2009). Therefore, we hypothesized that cerebellar astrocytes may demonstrate state-dependent Ca^{2+} dynamics throughout the sleep-wake cycle. To this end, we took advantage of the strong fluorescence intensity of cerebellar astrocytes in *Mlc1*-tTA; TetO-YCnano50 bigenic mouse line (Kanemaru et al., 2014).

To confirm astrocyte-specific expression of YCnano50 in the cerebellum, we performed immunostaining of astrocytes using S100β, an astrocyte-specific marker. The merged images show that YCnano50 was exclusively observed in cerebellar astrocytes in *Mlc1*-tTA; TetO-YCnano50 bigenic mice, and ectopic expression was not observed (Fig. 1A). Astrocytes in the cortex and hippocampus sparsely expressed YCnano50 as previously reported (Kanemaru et al., 2014). In this study, fiber photometry was used to record changes in astrocyte Ca^{2+} concentrations from head-fixed mice, as Y/C ratios (Fig. 1B). We first confirmed whether Y/C ratios

304 calculated from the YFP fluorescence and CFP fluorescence precisely reflect the
305 changes in astrocyte Ca^{2+} concentrations under our experimental conditions. For this
306 purpose, we analyzed changes in the Y/C ratio during tail pinch-induced locomotion in
307 mice, as it has previously been reported that astrocyte Ca^{2+} concentrations increase
308 with locomotion and the startle response in mice (Nimmerjahn et al., 2009; Srinivasan et
309 al., 2015; Bojarskaite et al., 2020). To deliver excitation light and collect fluorescence
310 signals from the cerebellum, a glass optical fiber was implanted into the cerebellum of
311 mice (Fig. 1C). Immediately after the tail pinch-induced locomotion, YFP fluorescence
312 and CFP fluorescence showed changes in opposite directions, resulting in an increase
313 in the Y/C ratio (Fig. 1D). The average Y/C ratio of the 10 secs immediately before the
314 tail pinch-induced locomotion was set to 1. The average Y/C ratio of the 10 secs
315 immediately after the tail pinch-induced locomotion was normalized, and a significant
316 increase in Y/C ratio upon locomotion was observed (n = 4 from three recording
317 sessions and one animal) (paired *t*-test: *, $p < 0.05$).

318 To assess the effect of YCnano50 expression in astrocytes, we examined
319 whether there are any signs of reactive astrocyte. We compared to the hippocampal
320 astrocytes which have sparce expression of YCnano50. There was no morphological
321 change and no signs of upregulation of glial fibrillary acidic protein (GFAP)
322 immunoreactivity between YCnano50-expressing astrocytes and intact astrocytes (Fig.
323 1F), indicating no toxic effects. To further confirm the effect of YCnano50 expressed in
324 bigenic mouse astrocytes and the effect of the head-fixed condition on sleep
325 architecture, we compared the duration of each sleep/wake episode and time spent in

each sleep/wake state during the light period (9:00–15:00) between the mice. To determine the sleep/wakefulness state of mice, EEG and EMG electrodes were implanted into their skulls and neck muscles. There were no significant differences between *Mlc1*-tTA; TetO-YCnano50 bigenic mice (six recording sessions and two animals) and *Mlc1*-tTA monogenic mice in the freely moving condition (six recording sessions and two animals) (Episode duration of wakefulness: Kruskal-Wallis: $F(3, 28) = 180.9$, $p = 0.10$, no significant difference [NS]; episode duration of NREM: Kruskal-Wallis: $F(3, 28) = 495.6$, $p < 0.05$, followed by multiple comparisons by the Bonferroni test: $p = 1$, NS; episode duration of REM: Kruskal-Wallis: $F(3, 21) = 92.2$, $p = 0.16$, NS; time spent in wakefulness: Kruskal-Wallis: $F(3, 28) = 11.1$, $p = 0.94$, NS; time spent in NREM: Kruskal-Wallis: $F(3, 28) = 23.1$, $p = 0.85$, NS; time spent in REM: Kruskal-Wallis: $F(3, 28) = 112.6$, $p = 0.27$, NS) (Table 1). On the other hand, the episode duration of NREM sleep was significantly reduced in mice in the head-fixed condition (without hypothalamus, 16 recording sessions and six animals) compared with mice in the freely moving condition (six recording sessions and two animals) (episode duration of NREM: Kruskal-Wallis: $F(3, 28) = 495.6$, $p < 0.05$, followed by multiple comparisons by the Bonferroni test: $p < 0.05$) (Table 1). However, no significant differences were observed between the other conditions.

State-dependent Ca^{2+} dynamics in cerebellar astrocytes

We next analyzed the dynamics of intracellular Ca^{2+} concentration in astrocytes during sleep/wakefulness states. Ca^{2+} signal dynamics were recorded during

the light period (9:00–15:00). Excitation light (20 Hz, 5 msec in width) was intermittently illuminated at random for 4 minutes. Y/C ratios gradually decreased during sleep, showing the lowest value during REM sleep, and instantaneously increased with awakening in *Mlc1*-tTA; TetO-YCnano50 mice (Fig. 1G). A decrease in Y/C ratio represents a decrease in Ca^{2+} concentration, as we have previously reported (Natsubori et al., 2017; Tsutsui-Kimura et al., 2017; Yoshida et al., 2020). In contrast, Y/C ratios did not change with sleep/wakefulness state in control *Mlc1*-tTA mice (Fig. 1H). The spectrogram of Y/C ratio in *Mlc1*-tTA; TetO-YCnano50 mice exhibited state-dependent changes at below ~0.25 Hz whereas small fluctuations at above ~0.25 Hz appeared even in Mlc1-tTA mice. These results indicate that signals below ~0.25Hz reflect state-dependent Ca^{2+} signals in astrocyte. Normalized Y/C ratios in wakefulness, NREM sleep, and REM sleep in cerebellar astrocytes of *Mlc1*-tTA; TetO-YCnano50 mice were 1.000 ± 0.001 (n = 66 episodes from 5 recording sessions and 3 animals), 0.988 ± 0.002 (n = 63 episodes from 5 recording sessions and 3 animals), and 0.944 ± 0.008 (n = 17 episodes from 3 recording sessions and 2 animals), respectively (Fig. 1I) (Kruskal-Wallis: $F(2, 143) = 56.68$, $p < 0.05$, followed by multiple comparison by the Bonferroni test: $p < 0.05$, effect size f = 1.07). In contrast, normalized Y/C ratios during wakefulness, NREM sleep, and REM sleep in cerebellar astrocytes of *Mlc1*-tTA mice were 1.000 ± 0.001 (n = 60 episodes from 5 recording sessions and 3 animals), 1.000 ± 0.001 (n = 70 episodes from 5 recording sessions and 3 animals), and 0.997 ± 0.001 (n = 33 episodes from 5 recording sessions and 3 animals), respectively (Fig. 1I) (Kruskal-Wallis: $F(2, 160) = 4.04$, $p = 0.13$, NS, effect size f = 0.17). These results

370 indicate that Ca^{2+} concentrations of cerebellar astrocytes change substantially with
371 sleep/wakefulness state in mice.

372 We next focused on Ca^{2+} dynamics during the transition between
373 sleep/wakefulness states (Fig. 1J). Y/C ratios gradually decreased after the onset of
374 NREM sleep following wakefulness. Sixteen seconds after the start of NREM sleep, Y/C
375 ratios significantly decreased compared with when mice were awake (n = 26 episodes
376 from three recording sessions and two animals) (one-way ANOVA: $F(11, 300) = 6.79$, p
377 < 0.05, followed by multiple comparisons by the Bonferroni test: $p < 0.05$ vs the fourth
378 epoch immediately before state transition). A slow decrease in Y/C ratios was also
379 observed in the transition from NREM sleep to REM sleep, but there was no significant
380 difference (n = 10 episodes from two recording sessions and two animals) (one-way
381 ANOVA: $F(11, 108) = 2.35$, $p < 0.05$, followed by multiple comparison by the Bonferroni
382 test: $p \geq 0.05$, NS). During the transition from NREM and REM sleep to wakefulness, the
383 Y/C ratio increased (from NREM to wake: n = 19 episodes from four recording sessions
384 and three animals; from REM to wake: n = 14 episodes from three recording sessions
385 and two animals) (from NREM to wake, one-way ANOVA: $F(11, 216) = 5.47$, $p < 0.05$,
386 followed by multiple comparisons by the Bonferroni test: $p < 0.05$ vs the fourth epoch
387 immediately before state transition; from REM to wake, one-way ANOVA: $F(11, 156) =$
388 12.87, $p < 0.05$, followed by multiple comparisons by the Bonferroni test: $p < 0.05$ vs the
389 fourth epoch immediately before state transition). However, the slopes were completely
390 different between from NREM to wakefulness and from REM to wakefulness. The slope
391 was calculated by dividing the difference in Y/C ratios immediately before and after the

392 transition by four seconds. The slope from REM to wakefulness (n = 14 episodes from
393 three recording sessions and two animals) was significantly larger than the slope from
394 NREM to wakefulness (Fig. 1K) (n = 19 episodes from 4 recording sessions and 3
395 animals) (unpaired *t*-test, $p < 0.05$). These results indicate that the signaling pathway
396 that increases intracellular Ca^{2+} concentrations might differ between from REM sleep
397 and from NREM sleep, although they do not appear to precede the four-second bin.
398 Next, correlation analysis was performed to investigate the association
399 between the episode duration of wakefulness, NREM, and REM, and changes in Ca^{2+}
400 concentrations (Fig. 1L–N). There was no significant correlation between wakefulness
401 and NREM sleep in either *Mlc1*-tTA; TetO-YCnano50 mice (wakefulness: n = 41
402 episodes from three recording sessions and two animals; NREM: n = 24 episodes from
403 three recording sessions and two animals) (wakefulness: $r = 0.14$, $p = 0.38$, NS; NREM:
404 $r = -0.23$, $p = 0.28$, NS) or in *Mlc1*-tTA mice (wakefulness: n = 46 episodes from five
405 recording sessions and three animals; NREM: n = 20 episodes from four recording
406 sessions and three animals) (wakefulness: $r = 0.13$, $p = 0.40$, NS; NREM: $r = -0.18$, $p =$
407 0.45, NS) (Fig. 1L, M). In contrast, there was a significant negative correlation between
408 the episode duration of REM and Y/C ratio in *Mlc1*-tTA; TetO-YCnano50 mice (Fig. 1N)
409 (n = 10 episodes from two recording sessions and two animals) ($r = -0.79$, $p < 0.05$),
410 which is in good agreement with the gradual decrease in Ca^{2+} level during REM sleep.
411 On the other hand, no significant correlation was observed in *Mlc1*-tTA mice (Fig. 1N) (n
412 = 12 episodes from two recording sessions and two animals) ($r = 0.09$, $p = 0.79$, NS).

These results indicate that Ca^{2+} concentration in cerebellar astrocytes decreases as REM sleep episode duration increases.

Correlation between EEG/EMG and Ca^{2+} signals in cerebellar astrocytes during sleep/wakefulness

Our results up to this point demonstrated that cerebellar astrocyte Ca^{2+} concentrations change dynamically with sleep/wakefulness state. Therefore, we next investigated whether Ca^{2+} fluctuations in cerebellar astrocytes also correlate with electrophysiological features during each sleep/wakefulness state. For this purpose, we investigated the association between Y/C ratios and cortical EEGs and EMGs during wakefulness, NREM, and REM sleep (50 recording sessions and three animals). Cortical EEGs were analyzed by dividing them into delta (1–5 Hz), theta (6–10 Hz), alpha (10–13 Hz), beta (13–25 Hz), and gamma (30–50 Hz) wave components. Regarding EMGs, their magnitudes were evaluated by calculating the rms. Then, their correlation with Y/C ratios was analyzed. During wakefulness, although Y/C ratios showed a significant negative correlation with alpha waves and EMG rms (Fig. 2A and 2D), the effect was weak (Fig. 2G), suggesting little cofluctuation of Ca^{2+} and electrophysiological signals during wakefulness. A negative correlation between EMG rms and Y/C ratio imply that Y/C ratio does not reflect simple motion-related signals. During NREM sleep, Y/C ratios were positively correlated with delta waves and EMG rms, and negatively correlated with theta, alpha, and beta waves (Fig. 2B, 2E, and 2H). During REM sleep, however, Y/C ratios demonstrated a positive correlation with delta,

435 alpha, and beta waves and EMG rms, and a negative correlation with theta waves (Fig.
436 2C, 2F, and 2I). Although this correlation analysis demonstrated significant differences,
437 no highly positive nor highly negative correlation was identified. A minor but statistically
438 significant correlation between cerebellar astrocyte Ca^{2+} concentrations and
439 electrophysiological features, particularly during sleep, was identified.
440
441 **State-dependent astrocyte Ca^{2+} dynamics among various brain regions**
442 We next assessed whether state-dependent changes in astrocyte Ca^{2+}
443 concentrations are observed not only in the cerebellum but also in other brain regions,
444 and whether the dynamics differ depending on the brain region. Fiber photometry
445 recordings were performed using a glass optical fiber from the cortex and hippocampus,
446 which have been reported to show diversity in neural activity corresponding to the
447 sleep/wakefulness state (Vyazovskiy et al., 2009; Grosmark et al., 2012; Watson et al.,
448 2016; Niethard et al., 2017), and from the hypothalamus and pons, which play a crucial
449 role in the regulation of sleep/wakefulness (Sakurai, 2007; Tsunematsu et al., 2014;
450 Hayashi et al., 2015; Weber et al., 2015; Weber and Dan, 2016; Scammell et al., 2017),
451 using *Mlc1*-tTA; TetO-YCnano50 mice. To deliver excitation light and collect
452 fluorescence signals, a glass optical fiber was implanted into the brains of mice (Fig.
453 3A). Hypothalamic recording of fiber-implanted in head-fixed *Mlc1*-tTA; TetO-YCnano50
454 mice (four recording sessions and two animals) demonstrated no differences in
455 sleep/wakefulness architecture compared with recordings from other brain regions in
456 head-fixed *Mlc1*-tTA; TetO-YCnano50 mice (16 recording sessions and six animals),

457 although the implanted optical fiber damages the brain and causes similar to glial
458 scarring around the optical fiber (Episode duration of wakefulness: Kruskal-Wallis: F(3,
459 28) = 180.9, p = 0.10, no significant difference [NS]; episode duration of NREM:
460 Kruskal-Wallis: F(3, 28) = 495.6, $p < 0.05$, followed by multiple comparisons by the
461 Bonferroni test: p = 1, NS; episode duration of REM: Kruskal-Wallis: F(3, 21) = 92.2, p =
462 0.16, NS; time spent in wakefulness: Kruskal-Wallis: F(3, 28) = 11.1, p = 0.94, NS; time
463 spent in NREM: Kruskal-Wallis: F(3, 28) = 23.1, p = 0.85, NS; time spent in REM:
464 Kruskal-Wallis: F(3, 28) = 112.6, p = 0.27, NS) (Table 1). Interestingly, astrocyte Ca^{2+}
465 levels dynamically changed depending on the sleep/wakefulness state throughout the
466 brain regions that were monitored, and significantly decreased in all areas during REM
467 sleep (Fig. 3B) (n = 69 wakefulness [W], 68 NREK sleep [NR], and 25 REM sleep [R]
468 episodes from five recording sessions and three animals in the cortex; n = 23 [W], 24
469 [NR], and 8 [R] episodes from two recording sessions and one animal in the
470 hippocampus; n = 60 [W], 69 [NR], and 20 [R] episodes from four recording sessions
471 and two animals in the hypothalamus; n = 40 [W], 43 [NR], and 34 [R] episodes from
472 two recording sessions and one animal in the pons) (Kruskal-Wallis: F(2, 159) = 29.3, p
473 < 0.05, effect size f = 0.47 in the cortex; Kruskal-Wallis: F(2, 52) = 39.1, $p < 0.05$, effect
474 size f = 1.34 in the hippocampus; Kruskal-Wallis: F(2, 146) = 30.0, $p < 0.05$, effect size f
475 = 0.80 in the hypothalamus; Kruskal-Wallis: F(2, 114) = 55.8, $p < 0.05$, effect size f =
476 1.13 in the pons, followed by multiple comparisons by the Bonferroni test: $p < 0.05$.).
477 However, significant decreases in Y/C ratios during NREM sleep were observed in the
478 cortex and hippocampus compared with that during wakefulness. In contrast, in the

hypothalamus and pons, no significant differences were observed between the Y/C ratios during wakefulness and NREM sleep, but Y/C ratios were significantly reduced during REM sleep compared with during NREM sleep. These results suggest that astrocyte Ca^{2+} levels are at a minimum during REM sleep, whereas they are high during wakefulness. This trend is consistent with that observed in the cerebellum. On the other hand, Ca^{2+} dynamics during NREM sleep vary depending on the brain region.

Further analyses during the sleep/wakefulness state transition clarified the variety of Ca^{2+} dynamics among the different brain regions (Fig. 3C). Focusing on the transition from wakefulness to NREM sleep, no significant changes were seen in the cortex, hypothalamus, and pons (n = 44 episodes from six recording sessions and three animals in the cortex; n = 38 episodes from two recording sessions and one animal in the hypothalamus; n = 17 episodes from one recording session and one animal in the pons) (Kruskal-Wallis: $F(11, 516) = 11.7$, $p = 0.39$, NS in the cortex; Kruskal-Wallis: $F(11, 444) = 3.2$, $p = 0.99$, NS in the hypothalamus; Kruskal-Wallis: $F(11, 192) = 7.3$, $p = 0.77$, NS in the pons). However, Y/C ratios gradually decreased in the hippocampus, and the difference became statistically significant after 24 seconds from state transition (n = 12 episodes from two recording sessions and one animal in the hippocampus) (Kruskal-Wallis: $F(11, 132) = 49.2$, $p < 0.05$, followed by multiple comparisons by the Bonferroni test: $p < 0.05$ vs the fourth epoch immediately before state transition in the hippocampus). A slow decrease in Y/C ratios in the hypothalamus and pons was observed from NREM to REM sleep (n = 6 episodes from two recording sessions and one animal in the hypothalamus; n = 8 episodes from two recording sessions and one

501 animal in the pons) (Kruskal-Wallis: $F(11, 60) = 39.9$, $p < 0.05$ in the hypothalamus;
502 Kruskal-Wallis: $F(11, 84) = 57.8$, $p < 0.05$ in the pons, followed by multiple comparisons
503 by the Bonferroni test: $p < 0.05$ vs the fourth epoch immediately before state transition),
504 whereas it was almost constant in the cortex but was increased in the hippocampus (n =
505 15 episodes from fix recording sessions and three animals in the cortex; n = 5 episodes
506 from two recording sessions and one animal in the hippocampus) (Kruskal-Wallis: $F(11,$
507 $168) = 0.98$, $p = 0.99$, NS in the cortex; Kruskal-Wallis: $F(11, 48) = 23.4$, $p < 0.05$,
508 followed by multiple comparisons by the Bonferroni test: NS vs the fourth epoch
509 immediately before state transition in the hippocampus). At the time of transition from
510 NREM sleep to wakefulness, Y/C ratios increased in the hippocampus (n = 12 episodes
511 from 2 recording sessions and 1 animal in the hippocampus) (Kruskal-Wallis: $F(11, 132)$
512 $= 89.3$, $p < 0.05$, followed by multiple comparisons by the Bonferroni test: $p < 0.05$ vs
513 the fourth epoch immediately before state transition in the hippocampus), but there was
514 no significant difference in the cortex, hypothalamus, and pons (n = 34 episodes from
515 seven recording sessions and three animals in the cortex; n = 25 episodes from two
516 recording sessions and one animal in the hypothalamus; n = 7 episodes from one
517 recording session and one animal in the pons) (Kruskal-Wallis: $F(11, 396) = 31.8$, $p <$
518 0.05, followed by multiple comparisons by the Bonferroni test: NS vs the fourth epoch
519 immediately before state transition in the cortex; Kruskal-Wallis: $F(11, 288) = 6.0$, $p =$
520 0.87, NS in the hypothalamus; Kruskal-Wallis: $F(11, 72) = 5.4$, $p = 0.91$, NS in the pons).
521 There were consistent increases immediately after the state change from REM sleep to
522 wakefulness in all brain regions that were monitored (n = 20 episodes from six recording

523 sessions and three animals in the cortex; n = 6 episodes from two recording sessions
524 and one animal in the hippocampus; n = 12 episodes from two recording sessions and
525 one animal in the hypothalamus; n = 12 episodes from two recording sessions and one
526 animal in the pons) (Kruskal-Wallis: $F(11, 228) = 109.5$, $p < 0.05$ in the cortex;
527 Kruskal-Wallis: $F(11, 60) = 55.5$, $p < 0.05$ in the hippocampus; Kruskal-Wallis: $F(11,$
528 $132) = 46.8$, $p < 0.05$ in the hypothalamus; Kruskal-Wallis: $F(11, 132) = 61.2$, $p < 0.05$ in
529 the pons, followed by multiple comparisons by the Bonferroni test: $p < 0.05$ vs the fourth
530 epoch immediately before state transition).

531 We also performed correlation analysis to investigate the association between
532 episode duration of REM and changes in Ca^{2+} concentration among the brain regions
533 (Fig. 3D). Changes in cortical and hippocampal Y/C ratios were not found to correlate
534 with episode duration of REM sleep (n = 22 episodes from six recording sessions and
535 three animals in the cortex; n = 6 episodes from two recording sessions and one animal
536 in the hippocampus) ($r = 0.28$, $p = 0.21$, NS in the cortex; $r = 0.61$, $p = 0.20$, NS in the
537 hippocampus). In the hypothalamus and pons, however, episode duration of REM sleep
538 and changes in Y/C ratios showed a significant negative correlation (n = 11 episodes
539 from two recording sessions and one animal in the hypothalamus; n = 5 episodes from
540 two recording sessions and one animal in the pons) ($r = -0.67$, $p < 0.05$ in the
541 hypothalamus; $r = -0.97$, $p < 0.05$ in the pons). These results suggest that the dynamics
542 of astrocyte Ca^{2+} concentration vary depending on the brain region. A longer episode
543 duration of REM sleep does not induce a further decrease in Ca^{2+} level in various
544 regions of the brain, such as in the cortex and hippocampus.

545 Next, we analyzed the correlation between electrophysiological features from
546 cortical EEGs and EMGs among the sleep/wakefulness states, and astrocyte Ca^{2+}
547 concentrations, using the same methods as in Figure 2. As we compared cortical EEGs
548 in this experiment, we focused on analyzing its correlation with the Ca^{2+} dynamics of
549 cortical astrocytes (6 recording sessions and 3 animals). During wakefulness, Y/C ratios
550 showed a weak negative correlation with alpha and beta waves, and a weak positive
551 correlation with gamma waves (Fig. 4A, 4D, and 4G). It was reported that an increase in
552 the power value of delta and alpha waves and a decrease in the power value of gamma
553 waves indicate a decrease in the arousal level during wakefulness (McGinley et al.,
554 2015). Cortical astrocyte Ca^{2+} levels appear to be low when mice are in quiet
555 wakefulness. During NREM sleep, cortical Y/C ratios were positively correlated with
556 delta waves, and were negatively correlated with theta, alpha, and beta waves,
557 consistent with those in the cerebellum (Fig. 4B, 4E, and 4H). During REM sleep,
558 however, Y/C ratios demonstrated a positive correlation with delta, and a negative
559 correlation with theta and alpha waves (Fig. 4C, 4F, and 4I). Although the Y scale has
560 become too large to see the trend due to outliers, EMG power and Y/C ratio were
561 positively correlated during both NREM and REM sleep (Fig. 4E and 4F). In this
562 correlation analysis, minor but significant differences were observed also in the
563 cerebellum. Compared with the results of the cerebellum, in the cortex, there was a
564 tendency towards a correlation between astrocyte Ca^{2+} concentrations and
565 electrophysiological features, not only during sleep but also during wakefulness.
566

Region-specific Ca^{2+} dynamics in astrocytes

We further quantified the regional differences in Ca^{2+} signals, including in the cerebellum. First, we quantified Ca^{2+} dynamics during each sleep/wakefulness episode, by categorizing the episodes into five states depending on the sleep/wakefulness state before and after each episode (Fig. 5A). Each episode was divided into five time-segments, and the average Ca^{2+} signal was calculated for each brain region (n = 6 recording sessions and three animals in the cortex; n = 2 recording sessions and one animal in the hippocampus; n = 4 recording sessions and two animals in the hypothalamus; n = 2 recording sessions and one animal in the pons; n = 5 recording sessions and three animals in the cerebellum).

Based on the results of Figure 3 and Figure 5A, there are likely to be three clusters in astrocyte Ca^{2+} signaling quality (Table 2). The first cluster is the cortex and hippocampus. Both cortical and hippocampal astrocytes showed a significant reduction in Ca^{2+} concentration during NREM sleep. No significant change was observed during the state transition from NREM sleep to REM sleep. In addition, no correlation was observed between astrocyte Ca^{2+} concentration and the duration of REM sleep episodes. The second cluster is the hypothalamus and pons. Astrocytes of both regions maintained their Ca^{2+} concentrations during NREM sleep, which decreased during REM. The third cluster is the cerebellum. In addition, Ca^{2+} signals during the state transition and during REM sleep episodes were completely identical between the hypothalamus and pons. Cerebellar astrocytes include characteristics of the other two clusters; i.e., their Ca^{2+} changes associated with sleep/wakefulness states tend to resemble those of

589 the cortex and hippocampus. However, as in the hypothalamus and brainstem, Ca^{2+}
590 changes negatively correlated with the durations of REM episodes.

591 Next, we analyzed the extent to which astrocyte Ca^{2+} signals can predict the
592 ongoing sleep/wakefulness state, and whether there are any differences in decoding
593 performance among the brain regions. For this purpose, average Ca^{2+} signals were
594 computed in each epoch, and a linear classifier was trained with 4-fold cross validation
595 (Tsunematsu et al., 2020). The decoding performance based on Y/C ratio of
596 hippocampus and cerebellum in *Mlc1*-tTA; TetO-YCnano50 mice was significantly
597 higher than that in *Mlc1*-tTA mice (Fig. 5B; $p < 0.05$, one-way ANOVA). This result
598 indicates that hippocampal and cerebellar astrocyte activity demonstrate
599 sleep/wakefulness state-dependency. In addition, we also clarified the differences in
600 decoding performance among the different brain regions. Decoding performance of the
601 cerebellum was significantly higher than that of the cortex (Fig. 5B; $p < 0.05$, one-way
602 ANOVA). Thus, the physiological role of astrocytes in sleep/wakefulness might vary
603 depending on the brain region.
604

Discussion

In the present study, we analyzed astrocyte Ca^{2+} dynamics during different sleep/wakefulness states among various brain regions. We demonstrated that astrocyte Ca^{2+} concentrations decreased during sleep, reached a minimum during REM sleep, and increased during wakefulness in all brain regions that were recorded. Further analyses indicated that there are at least three astrocyte clusters, comprising astrocytes from different brain regions. Although the association between changes in astrocyte Ca^{2+} concentrations and sleep/wakefulness were consistent in general among the brain regions, we found that detailed Ca^{2+} dynamics varies depending on the brain region.

Technical differences compared with other similar studies

Several recent studies measuring astrocyte Ca^{2+} concentrations during sleep/wakefulness states have been reported (Bojarskaite et al., 2020; Ingiosi et al., 2020). The results of these studies are in good agreement with our results showing that astrocyte Ca^{2+} concentrations/signals decrease during sleep and increase during wakefulness. However, there are several differences. We showed a decrease in Ca^{2+} concentration in the cortex during NREM sleep, which is consistent with previous studies (Bojarskaite et al., 2020; Ingiosi et al., 2020). However, our present study demonstrated that no increase in Ca^{2+} level was observed during the transition from wakefulness to NREM sleep in the cortex, which is inconsistent with a recent study (Ingiosi et al., 2020). Moreover, both papers reported that the Ca^{2+} concentration once increased after transition from sleep to wakefulness then slightly decreased within 15

627 seconds. Our study, however, did not show a Ca^{2+} overshoot in any of the recorded
628 brain regions, even though we showed 32 seconds of data post-transition. These
629 differences may be due to differences experimental conditions.

630 The first difference is the Ca^{2+} sensor that was used. We used the
631 fluorescence resonance energy transfer-based, ultrasensitive genetically encoded Ca^{2+}
632 indicator YCnano50 (Horikawa et al., 2010). On the other hand, other studies have used
633 GCaMP6f (Chen et al., 2013). YCnano50 has high Ca^{2+} affinity (Kd = 50 nM) compared
634 with GCaMP6f (Kd = 375 nM). Because of the ability of YCnano50 to detect subtle basal
635 changes in the Ca^{2+} concentrations, our study was able to clarify the distinct differences
636 in astrocyte Ca^{2+} concentrations between NREM and REM sleep.

637 The second difference is the method of expression of the Ca^{2+} sensor.
638 Previous studies expressed the sensor using an adeno-associated virus, whereas we
639 used *Mlc1*-tTA; TetO-YCnano50 bigenic mice to express the sensor in an
640 astrocyte-specific manner. Because we used genetically modified mice rather than virus
641 infection, the expression level and pattern of YCnano50 were constant among mice,
642 and hence consistent data could be obtained. Although the sensors were substantially
643 expressed in the cerebellum, pons, and hypothalamus, the sparce expression was
644 observed in the cortex, and hippocampus in the genetically modified mice. It cannot
645 exclude the possibility that the expression level of YCnano50 have made a difference
646 from previous studies.

647 The third difference is the optical imaging approach that was used. As we
648 recorded Ca^{2+} levels in astrocytes using the fiber photometry system, it was possible to

649 analyze deeper regions of the brain, such as the hypothalamus and pons. However, our
650 method only enables the measurement of the sum of changes in Ca^{2+} concentrations of
651 cells. Our previous fiber photometry experiments using the same fiber optics and similar
652 light intensities demonstrated that the detection limit is at a depth of approximately 700
653 μm (Natsubori et al., 2017). Assuming a tissue refractive index of 1.5, we detected
654 signals with a diameter of approximately 800 μm at the 700 μm from tips of fiber optics.
655 It indicates that the sum of Ca^{2+} signals of multiple nuclei and sub-regions were
656 recorded although signals from specific brain region were detected at least. The Ca^{2+}
657 dynamics at the nuclei, single-cell and subcellular level remains unknown. In recording
658 from deep region, especially from the hypothalamus, the implanted optical fiber
659 damaged the tissue and caused similar to glial scaring. Although there was no effect on
660 the sleep/wakefulness state, the conclusion should be handled with care. Further
661 detailed analyses are needed.

662 Nevertheless, taking advantage of our method, we succeeded in comparing
663 astrocyte Ca^{2+} dynamics among various brain regions.

664

665 **Correlation between electrophysiological features and astrocyte Ca^{2+}**
666 **concentrations**

667 Here, we investigated the correlation of cerebellar and cortical astrocyte Ca^{2+}
668 concentrations with cortical oscillations. During NREM sleep, we found that consistent
669 negative correlations between Y/C ratio and alpha/beta power across recordings in the
670 cerebellum and the cortex. Although beta oscillations have long been implicated in

671 long-range communication between brain regions (Fries, 2015), the function of such
672 middle frequency oscillations during NREM sleep remains unclear. During REM sleep,
673 we found negative correlations between Y/C ratio and theta power. Because theta
674 power is a prominent biomarkers of REM sleep (Brown et al., 2012), astrocytic Ca^{2+}
675 signals in the cortex and the cerebellum may reflect the depth and/or quality of REM
676 sleep.
677
678 **Possible mechanisms regulating astrocyte Ca^{2+} concentrations**
679 We observed similar Ca^{2+} concentration changes in different brain regions.
680 This was an interesting result that was inconsistent with neural activity. For instance,
681 cortical neurons activate during wakefulness and REM sleep (Vyazovskiy et al., 2009;
682 Watson et al., 2016; Niethard et al., 2017), hippocampal neurons fire less during REM
683 sleep (Grosmark et al., 2012; Miyawaki and Diba, 2016), and an increase in the firing
684 rate in the brainstem is observed during REM sleep (Hobson et al., 1975; Weber et al.,
685 2015; Tsunematsu et al., 2020). Thus, it has been reported that neural activity patterns
686 vary depending on the brain region.
687 It has also been reported that Ca^{2+} concentrations are affected by G-protein
688 coupled receptors (GPCRs) expressed in astrocytes via neurotransmitter release that
689 accompanies neural activity. In general, the activation of astrocyte GPCRs increases
690 astrocyte Ca^{2+} levels (Cornell-Bell et al., 1990; Takata et al., 2011; Jacob et al., 2014;
691 Corkrum et al., 2020), although in some instances a decrease in Ca^{2+} level has been
692 reported (Jennings et al., 2017). However, we observed global Ca^{2+} concentration

693 changes, and therefore it is possible that a neurotransmitter that shows varying release
694 patterns throughout the brain during different sleep/wakefulness states controls
695 astrocyte Ca^{2+} concentration. Noradrenaline has been reported to increase astrocyte
696 Ca^{2+} levels (Bekar et al., 2008; Paukert et al., 2014; Oe et al., 2020). Noradrenergic
697 neurons located in the locus coeruleus project to the entire brain. Changes in firing rates
698 of noradrenergic neurons showed a similar pattern to the Ca^{2+} dynamics of astrocytes
699 (Takahashi et al., 2010; Tsujino et al., 2013). Taken together, noradrenaline released
700 from noradrenergic neurons during wakefulness might increase astrocyte Ca^{2+}
701 concentrations throughout the brain. In addition, considering that astrocyte Ca^{2+} levels
702 gradually decrease during REM sleep, noradrenaline might also act as a volume
703 transmitter, because microdialysis studies have reported that the concentration of
704 noradrenaline in the brain decreases during sleep (Park, 2002; Bellesi et al., 2016). It
705 has been reported that not only noradrenaline but also glutamate, acetylcholine, and
706 gamma-aminobutyric acid increase astrocyte Ca^{2+} levels (Cornell-Bell et al., 1990; Kang
707 et al., 1998; Araque et al., 2002; Sun et al., 2013; Perea et al., 2016). Thus, the effects
708 of these neurotransmitters as well as neuropeptides which regulate sleep/wakefulness
709 state should be elucidated.
710
711 **Possible heterogeneity of astrocytes among various brain regions**
712 The results of this study surprisingly implicate that astrocytes in different brain
713 regions may have different functions in sleep/wakefulness. Based on our results, we
714 classified astrocytes into the following three clusters: cluster 1, astrocytes in the cortex

715 and hippocampus; cluster 2, astrocytes in the hypothalamus and pons; and cluster 3,
716 astrocytes in the cerebellum.

717 Astrocytes have recently been clarified to be a heterogeneous population.
718 Transcriptional analyses have demonstrated that astrocyte gene expression patterns
719 differ among and within brain regions and can be classified into several types (Chai et
720 al., 2017; Zeisel et al., 2018; Batiuk et al., 2020; Bayraktar et al., 2020). The gene
721 expression patterns indicated that cortical and hippocampal astrocytes have similar
722 transcriptional profiles (Morel et al., 2017; Lozzi et al., 2020). In contrast, Bergmann glial
723 cells are a type of cerebellar astrocyte with unique morphological and transcriptional
724 characteristics, although there are other glial cells, i.e., velate astrocytes, in the
725 cerebellum. Bergmann glial cells express Ca^{2+}-permeable AMPA receptors composed
726 of the GluA1 and GluA4 subunits (Saab et al., 2012), implying that they have different
727 intracellular Ca^{2+} dynamics. Our results may explain part of the differences in the
728 functions of astrocytes depending on the brain region, as well as the differences in their
729 cellular transcriptomes. In our study, the number of mice in which the hippocampus and
730 pons was analyzed was limited, although the effect size was 1.34 and 1.13, respectively.
731 Furthermore, the effect size calculated from the data of the cortex was 0.47, indicating a
732 medium effect. Thus, further analyses are required before making any definite
733 conclusions.

734 Decoding performance for ongoing sleep/wakefulness states was significantly
735 higher in the hippocampus and cerebellum of *Mlc1*-tTA; TetO-YCnano50 mice than
736 *Mlc1*-tTA mice, suggesting that astrocyte Ca^{2+} dynamics might not only show

737 state-dependent fluctuation, but also contribute to the control of the sleep/wakefulness
738 state itself. Further research should be performed with the caveat that astrocyte
739 functions in sleep/wakefulness states might vary among different brain regions.
740

741 **Figure legends**

742 **Figure 1. Astrocyte Ca^{2+} dynamics in the cerebellum during sleep/wakefulness**
743 **states of mice**

744 (A) Immunohistochemical analysis demonstrating that YCnano50 is specifically
745 expressed in cerebellar astrocytes in the *Mlc1*-tTA; TetO-YCnano50 bigenic mouse
746 brain. Left, YFP fluorescence of YCnano50-positive cells (green). Middle,
747 S100β-immunoreactive astrocytes (red). Left, merged image (yellow). Scale bar = 40
748 μm. GL, granule cell layer; ML, molecular layer; PL, Purkinje cell layer. (B) Schematic
749 drawing showing the fiber photometry system used in this study. Fluorescence emission
750 is applied from the LED light source. Yellow and cyan fluorescence signals were
751 corrected by bandpass filters and enhanced by photomultipliers (PMT). (C) The location
752 of the glass optical fiber, which was implanted in the cerebellum of *Mlc1*-tTA;
753 TetO-YCnano50 bigenic mice (6.0 mm posterior, 1.0 mm lateral from bregma, 0.5 mm
754 depth from the brain surface). Scale bar = 1 mm. (D) Example of Y/C ratios (top) and
755 corresponding intensity changes of yellow and cyan fluorescence (bottom) recorded
756 during tail pinch-induced locomotion in *Mlc1*-tTA; TetO-YCnano50 bigenic mice. The
757 arrows indicate the timing of the tail pinch. (E) Box plot summarizing the data from D.
758 The Y/C ratios during locomotion were normalized using the Y/C ratio at 10 sec
759 immediately before the locomotion set as 1. ∗, $p < 0.05$. (F) Comparison of GFAP
760 immunoreactivity (red) with (arrowheads) or without (arrows) YCnano50 expression
761 (green) in the hippocampal astrocytes. Scale bar = 15 μm. (G and H) Representative
762 traces of EEG, EEG power density spectrum, EMG, cerebellar astrocyte Ca^{2+} signals

(Y/C ratio), and Y/C ratio spectrogram in *Mlc1*-tTA; TetO-YCnano50 bigenic mice (G) and *Mlc1*-tTA monogenic mice (H). (I) Box plot summarizing the data from G and H. Y/C ratios were normalized to the value of each episode, with the average value of awakening set as 1. ∗, $p < 0.05$. (J) Y/C ratios during the transitions between the sleep/wakefulness states. Transitions occurred at time 0. Data are from 4-sec intervals characterized by state transitions. The line graph with the colored circles and gray circles are a summary of the data from *Mlc1*-tTA; TetO-YCnano50 bigenic mice and *Mlc1*-tTA monogenic mice, respectively. ∗, $p < 0.05$ vs the fourth epoch immediately before the state transition. (K) Bar graph representing the slope of the Y/C ratio of mice at the time of awakening from NREM sleep and REM sleep. ∗, $p < 0.05$. (L, M, and N) Analyses of the correlation between Y/C ratios and episode duration of wakefulness (L), NREM sleep (M), and REM sleep (N). Colored circles and gray circles indicate the summary of data from *Mlc1*-tTA; TetO-YCnano50 bigenic mice and *Mlc1*-tTA monogenic mice, respectively. NR, NREM sleep; R, REM sleep; W, wakefulness. Values are shown as means ± SEM.

Figure 2. Correlation between EEG/EMG and cerebellar astrocytic Ca^{2+} signals during different sleep/wakefulness states

(A, B, and C) Correlation analyses between normalized (z-scored) cerebellar astrocytic Y/C ratios, and normalized (z-scored) EEG power densities in the delta (1–5 Hz), theta (6–10 Hz), alpha (10–13 Hz), beta (13–25 Hz), and gamma (30–50 Hz) waves during wakefulness (A), NREM sleep (B), and REM sleep (C). (D, E, and F) Correlation

785 analyses between normalized Y/C ratios and normalized rms of EMG during
786 wakefulness (D), NREM sleep (E), and REM sleep (F). The data in this figure were
787 analyzed in 1 sec bin sizes. (G, H, and I) Bar graphs showing correlation coefficients
788 summarizing the data from A to F. The correlation coefficient of each recording was
789 cross-validated by splitting the data into the first and second halves.
790

791 **Figure 3. Astrocyte Ca^{2+} dynamics during different sleep/wakefulness states in**
792 **various brain regions**
793 (A) Images indicating the location of the glass optical fiber, which was implanted into the
794 cortex, hippocampus, hypothalamus, and pons. Arrows indicates the tip of the optical
795 fiber. Scale bar = 500 μm (cortex and hippocampus), and 1 mm (hypothalamus and
796 pons). (B) Box plot summarizing the data of the normalized Y/C ratios obtained from the
797 cortex, hippocampus, hypothalamus, and pons. ∗, $p < 0.05$. (C) Y/C ratios for the
798 transition of sleep/wakefulness states in multiple brain regions. Black filled symbols
799 indicate $p < 0.05$ vs. the fourth epoch immediately before state transition in each brain
800 region. (D) Correlation analyses between episode durations of REM sleep and Y/C
801 ratios in the cortex, hippocampus, hypothalamus, and pons. NR, NREM sleep; R, REM
802 sleep; W, wakefulness. Values are represented as means ± SEM.
803

804 **Figure 4. Correlation of EEG/EMG and cortical astrocyte Ca^{2+} signals during**
805 **different sleep/wakefulness states**

(A, B, and C) Correlation analyses between normalized (z-scored) Y/C ratios from the cortex and normalized (z-scored) EEG power densities in the delta (1–5 Hz), theta (6–10 Hz), alpha (10–13 Hz), beta (13–25 Hz), and gamma (30–50 Hz) waves during wakefulness (A), NREM sleep (B), and REM sleep (C). (D, E, and F) Correlation analyses between normalized Y/C ratios and normalized rms of EMG during wakefulness (D), NREM sleep (E), and REM sleep (F). The data in this figure were analyzed using 1 sec bin sizes. (G, H, and I) Bar graphs showing correlation coefficients summarizing the data from A to F. The correlation coefficient of each recording was cross-validated by splitting the data into the first and second halves.

Figure 5. Dynamics of Ca^{2+} signals during different sleep/wakefulness states and different brain regions

(A) The mean profiles of Ca^{2+} signals during time-normalized episodes. In each panel, the duration of each episode was segmented into 5 bins and the mean normalized Y/C ratios were computed in various brain regions. (B) Decoding performance of Ca^{2+} signals for different sleep/wakefulness states among various brain regions. *, $p < 0.05$, $F(5, 17) = 6.10$, one-way ANOVA with the *post-hoc* HSD test.

824 **References**

825

826 Allen NJ (2014) Astrocyte regulation of synaptic behavior. Annu Rev Cell Dev Biol
827 30:439-463.
828 Allen NJ, Eroglu C (2017) Cell Biology of Astrocyte-Synapse Interactions. Neuron
829 96:697-708.
830 Araque A, Martin ED, Perea G, Arellano JI, Buno W (2002) Synaptically released
831 acetylcholine evokes Ca2+ elevations in astrocytes in hippocampal slices. J
832 Neurosci 22:2443-2450.
833 Araque A, Carmignoto G, Haydon PG, Oliet SH, Robitaille R, Volterra A (2014)
834 Gliotransmitters travel in time and space. Neuron 81:728-739.
835 Batiuk MY, Martirosyan A, Wahis J, de Vin F, Marneffe C, Kusserow C, Koeppen J,
836 Viana JF, Oliveira JF, Voet T, Ponting CP, Belgard TG, Holt MG (2020)
837 Identification of region-specific astrocyte subtypes at single cell resolution. Nat
838 Commun 11:1220.
839 Bayraktar OA et al. (2020) Astrocyte layers in the mammalian cerebral cortex revealed
840 by a single-cell in situ transcriptomic map. Nat Neurosci 23:500-509.
841 Bekar LK, He W, Nedergaard M (2008) Locus coeruleus alpha-adrenergic-mediated
842 activation of cortical astrocytes in vivo. Cereb Cortex 18:2789-2795.
843 Bellesi M, Tononi G, Cirelli C, Serra PA (2016) Region-Specific Dissociation between
844 Cortical Noradrenaline Levels and the Sleep/Wake Cycle. Sleep 39:143-154.
845 Beppu K, Sasaki T, Tanaka KF, Yamanaka A, Fukazawa Y, Shigemoto R, Matsui K
846 (2014) Optogenetic countering of glial acidosis suppresses glial glutamate
847 release and ischemic brain damage. Neuron 81:314-320.
848 Bojarskaite L, Bjornstad DM, Pettersen KH, Cunen C, Hermansen GH, Abjorsbraten KS,
849 Chambers AR, Sprengel R, Vervaeke K, Tang W, Enger R, Nagelhus EA (2020)
850 Astrocytic Ca(2+) signaling is reduced during sleep and is involved in the
851 regulation of slow wave sleep. Nat Commun 11:3240.
852 Boor PK, de Groot K, Waisfisz Q, Kamphorst W, Oudejans CB, Powers JM, Pronk JC,
853 Scheper GC, van der Knaap MS (2005) MLC1: a novel protein in distal astroglial
854 processes. J Neuropathol Exp Neurol 64:412-419.
855 Brown RE, Basheer R, McKenna JT, Strecker RE, McCarley RW (2012) Control of

856 Sleep and Wakefulness. Physiological Reviews 92:1087-1187.
857 Chai H, Diaz-Castro B, Shigetomi E, Monte E, Octeau JC, Yu X, Cohn W, Rajendran PS,
858 Vondriska TM, Whitelegge JP, Coppola G, Khakh BS (2017) Neural
859 Circuit-Specialized Astrocytes: Transcriptomic, Proteomic, Morphological, and
860 Functional Evidence. Neuron 95:531-549 e539.
861 Chen TW, Wardill TJ, Sun Y, Pulver SR, Renninger SL, Baohan A, Schreiter ER, Kerr
862 RA, Orger MB, Jayaraman V, Looger LL, Svoboda K, Kim DS (2013)
863 Ultrasensitive fluorescent proteins for imaging neuronal activity. Nature
864 499:295-300.
865 Clasadonte J, Scemes E, Wang Z, Boison D, Haydon PG (2017) Connexin 43-Mediated
866 Astroglial Metabolic Networks Contribute to the Regulation of the Sleep-Wake
867 Cycle. Neuron 95:1365-1380 e1365.
868 Corkrum M, Covelo A, Lines J, Bellocchio L, Pisansky M, Loke K, Quintana R, Rothwell
869 PE, Lujan R, Marsicano G, Martin ED, Thomas MJ, Kofuji P, Araque A (2020)
870 Dopamine-Evoked Synaptic Regulation in the Nucleus Accumbens Requires
871 Astrocyte Activity. Neuron 105:1036-1047 e1035.
872 Cornell-Bell AH, Finkbeiner SM, Cooper MS, Smith SJ (1990) Glutamate induces
873 calcium waves in cultured astrocytes: long-range glial signaling. Science
874 247:470-473.
875 Faul F, Erdfelder E, Lang AG, Buchner A (2007) G*Power 3: a flexible statistical power
876 analysis program for the social, behavioral, and biomedical sciences. Behav Res
877 Methods 39:175-191.
878 Filosa JA, Naskar K, Perfume G, Iddings JA, Biancardi VC, Vatta MS, Stern JE (2012)
879 Endothelin-mediated calcium responses in supraoptic nucleus astrocytes
880 influence magnocellular neurosecretory firing activity. J Neuroendocrinol
881 24:378-392.
882 Florian C, Vecsey CG, Halassa MM, Haydon PG, Abel T (2011) Astrocyte-derived
883 adenosine and A1 receptor activity contribute to sleep loss-induced deficits in
884 hippocampal synaptic plasticity and memory in mice. J Neurosci 31:6956-6962.
885 Frank MG (2019) The Role of Glia in Sleep Regulation and Function. Handb Exp
886 Pharmacol 253:83-96.
887 Fries P (2015) Rhythms for Cognition: Communication through Coherence. Neuron
888 88:220-235.

889 Gourine AV, Kasymov V, Marina N, Tang F, Figueiredo MF, Lane S, Teschemacher AG,
890 Spyer KM, Deisseroth K, Kasparov S (2010) Astrocytes control breathing
891 through pH-dependent release of ATP. Science 329:571-575.
892 Grosmark AD, Mizuseki K, Pastalkova E, Diba K, Buzsáki G (2012) REM sleep
893 reorganizes hippocampal excitability. Neuron 75:1001-1007.
894 Halassa MM, Florian C, Fellin T, Munoz JR, Abel T, Haydon PG, Frank MG (2009)
895 Astrocytic modulation of sleep homeostasis and cognitive consequences of
896 sleep loss. Neuron 61:213-219.
897 Hayashi Y, Kashiwagi M, Yasuda K, Ando R, Kanuka M, Sakai K, Itohara S (2015) Cells
898 of a common developmental origin regulate REM/non-REM sleep
899 andwakefulness in mice. Science 350:957-962.
900 Hobson JA, McCarley RW, Wyzinski PW (1975) Sleep cycle oscillation: reciprocal
901 discharge by two brainstem neuronal groups. Science 189:55-58.
902 Holmstrom KM, Marina N, Baev AY, Wood NW, Gourine AV, Abramov AY (2013)
903 Signalling properties of inorganic polyphosphate in the mammalian brain. Nat
904 Commun 4:1362.
905 Hoogland TM, Kuhn B, Gobel W, Huang W, Nakai J, Helmchen F, Flint J, Wang SS
906 (2009) Radially expanding transglial calcium waves in the intact cerebellum.
907 Proc Natl Acad Sci U S A 106:3496-3501.
908 Horikawa K, Yamada Y, Matsuda T, Kobayashi K, Hashimoto M, Matsu-ura T, Miyawaki
909 A, Michikawa T, Mikoshiba K, Nagai T (2010) Spontaneous network activity
910 visualized by ultrasensitive Ca(2+) indicators, yellow Cameleon-Nano. Nat
911 Methods 7:729-732.
912 Ingiosi AM, Hayworth CR, Harvey DO, Singletary KG, Rempe MJ, Wisor JP, Frank MG
913 (2020) A Role for Astroglial Calcium in Mammalian Sleep and Sleep Regulation.
914 Curr Biol.
915 Jacob PF, Vaz SH, Ribeiro JA, Sebastiao AM (2014) P2Y1 receptor inhibits GABA
916 transport through a calcium signalling-dependent mechanism in rat cortical
917 astrocytes. Glia 62:1211-1226.
918 Jennings A, Tyurikova O, Bard L, Zheng K, Semyanov A, Henneberger C, Rusakov DA
919 (2017) Dopamine elevates and lowers astroglial Ca(2+) through distinct
920 pathways depending on local synaptic circuitry. Glia 65:447-459.
921 Kanemaru K, Sekiya H, Xu M, Satoh K, Kitajima N, Yoshida K, Okubo Y, Sasaki T,

922 Moritoh S, Hasuwa H, Mimura M, Horikawa K, Matsui K, Nagai T, Iino M, Tanaka
923 KF (2014) In vivo visualization of subtle, transient, and local activity of astrocytes
924 using an ultrasensitive Ca(2+) indicator. Cell Rep 8:311-318.
925 Kang J, Jiang L, Goldman SA, Nedergaard M (1998) Astrocyte-mediated potentiation of
926 inhibitory synaptic transmission. Nat Neurosci 1:683-692.
927 Liu D, Dan Y (2019) A Motor Theory of Sleep-Wake Control: Arousal-Action Circuit.
928 Annu Rev Neurosci 42:27-46.
929 Lozzi B, Huang TW, Sardar D, Huang AY, Deneen B (2020) Regionally Distinct
930 Astrocytes Display Unique Transcription Factor Profiles in the Adult Brain. Front
931 Neurosci 14:61.
932 Magistretti PJ, Allaman I (2018) Lactate in the brain: from metabolic end-product to
933 signalling molecule. Nat Rev Neurosci 19:235-249.
934 McGinley MJ, Vinck M, Reimer J, Batista-Brito R, Zagha E, Cadwell CR, Tolias AS,
935 Cardin JA, McCormick DA (2015) Waking State: Rapid Variations Modulate
936 Neural and Behavioral Responses. Neuron 87:1143-1161.
937 Min R, Nevian T (2012) Astrocyte signaling controls spike timing-dependent depression
938 at neocortical synapses. Nat Neurosci 15:746-753.
939 Miyawaki H, Diba K (2016) Regulation of Hippocampal Firing by Network Oscillations
940 during Sleep. Curr Biol 26:893-902.
941 Morel L, Chiang MSR, Higashimori H, Shoneye T, Iyer LK, Yelick J, Tai A, Yang Y (2017)
942 Molecular and Functional Properties of Regional Astrocytes in the Adult Brain. J
943 Neurosci 37:8706-8717.
944 Natsubori A, Tsutsui-Kimura I, Nishida H, Bouchekioua Y, Sekiya H, Uchigashima M,
945 Watanabe M, de Kerchove d'Exaerde A, Mimura M, Takata N, Tanaka KF (2017)
946 Ventrolateral Striatal Medium Spiny Neurons Positively Regulate Food-Incentive,
947 Goal-Directed Behavior Independently of D1 and D2 Selectivity. J Neurosci
948 37:2723-2733.
949 Navarrete M, Araque A (2010) Endocannabinoids potentiate synaptic transmission
950 through stimulation of astrocytes. Neuron 68:113-126.
951 Niethard N, Burgalossi A, Born J (2017) Plasticity during Sleep Is Linked to Specific
952 Regulation of Cortical Circuit Activity. Front Neural Circuits 11:65.
953 Nimmerjahn A, Mukamel EA, Schnitzer MJ (2009) Motor behavior activates Bergmann
954 glial networks. Neuron 62:400-412.

955 Oe Y, Wang X, Patriarchi T, Konno A, Ozawa K, Yahagi K, Hirai H, Tian L, McHugh TJ,
956 Hirase H (2020) Distinct temporal integration of noradrenaline signaling by
957 astrocytic second messengers during vigilance. Nat Commun 11:471.
958 Park SP (2002) In vivo microdialysis measures of extracellular norepinephrine in the rat
959 amygdala during sleep-wakefulness. J Korean Med Sci 17:395-399.
960 Paukert M, Agarwal A, Cha J, Doze VA, Kang JU, Bergles DE (2014) Norepinephrine
961 controls astroglial responsiveness to local circuit activity. Neuron 82:1263-1270.
962 Pelluru D, Konadhode RR, Bhat NR, Shiromani PJ (2016) Optogenetic stimulation of
963 astrocytes in the posterior hypothalamus increases sleep at night in C57BL/6J
964 mice. Eur J Neurosci 43:1298-1306.
965 Perea G, Gomez R, Mederos S, Covelo A, Ballesteros JJ, Schlosser L,
966 Hernandez-Vivanco A, Martin-Fernandez M, Quintana R, Rayan A, Diez A,
967 Fuenzalida M, Agarwal A, Bergles DE, Bettler B, Manahan-Vaughan D, Martin
968 ED, Kirchhoff F, Araque A (2016) Activity-dependent switch of GABAergic
969 inhibition into glutamatergic excitation in astrocyte-neuron networks. Elife 5.
970 Poskanzer KE, Yuste R (2016) Astrocytes regulate cortical state switching in vivo.
971 Proceedings of the National Academy of Sciences of the United States of
972 America 2016:1-10.
973 Radulovacki M, Virus RM, Djuricic-Nedelson M, Green RD (1984) Adenosine analogs
974 and sleep in rats. J Pharmacol Exp Ther 228:268-274.
975 Saab AS, Neumeyer A, Jahn HM, Cupido A, Simek AA, Boele HJ, Scheller A, Le Meur K,
976 Gotz M, Monyer H, Sprengel R, Rubio ME, Deitmer JW, De Zeeuw CI, Kirchhoff
977 F (2012) Bergmann glial AMPA receptors are required for fine motor
978 coordination. Science 337:749-753.
979 Sakurai T (2007) The neural circuit of orexin (hypocretin): maintaining sleep and
980 wakefulness. Nature reviews Neuroscience 8:171-181.
981 Sasaki T, Beppu K, Tanaka KF, Fukazawa Y, Shigemoto R (2012) Application of an
982 optogenetic byway for perturbing neuronal activity via glial photostimulation.
983 Savtchouk I, Volterra A (2018) Gliotransmission: Beyond Black-and-White. J Neurosci
984 38:14-25.
985 Scammell TE, Arrigoni E, Lipton JO (2017) Neural Circuitry of Wakefulness and Sleep.
986 Neuron 93:747-765.
987 Sofroniew MV, Vinters HV (2010) Astrocytes: biology and pathology. Acta Neuropathol

119:7-35.

Srinivasan R, Huang BS, Venugopal S, Johnston AD, Chai H, Zeng H, Golshani P, Khakh BS (2015) Ca(2+) signaling in astrocytes from Ip3r2(-/-) mice in brain slices and during startle responses in vivo. Nat Neurosci 18:708-717.

Sun W, McConnell E, Pare JF, Xu Q, Chen M, Peng W, Lovatt D, Han X, Smith Y, Nedergaard M (2013) Glutamate-dependent neuroglial calcium signaling differs between young and adult brain. Science 339:197-200.

Takahashi K, Kayama Y, Lin JS, Sakai K (2010) Locus coeruleus neuronal activity during the sleep-waking cycle in mice. Neuroscience 169:1115-1126.

Takata N, Mishima T, Hisatsune C, Nagai T, Ebisui E, Mikoshiba K, Hirase H (2011) Astrocyte calcium signaling transforms cholinergic modulation to cortical plasticity in vivo. J Neurosci 31:18155-18165.

Tanaka KF, Ahmari SE, Leonardo ED, Richardson-Jones JW, Budreck EC, Scheiffele P, Sugio S, Inamura N, Ikenaka K, Hen R (2010) Flexible Accelerated STOP Tetracycline Operator-knockin (FAST): a versatile and efficient new gene modulating system. Biol Psychiatry 67:770-773.

Tanaka KF, Matsui K, Sasaki T, Sano H, Sugio S, Fan K, Hen R, Nakai J, Yanagawa Y, Hasuwa H, Okabe M, Deisseroth K, Ikenaka K, Yamanaka A (2012) Expanding the repertoire of optogenetically targeted cells with an enhanced gene expression system. Cell Rep 2:397-406.

Teijido O, Casaroli-Marano R, Kharkovets T, Aguado F, Zorzano A, Palacin M, Soriano E, Martinez A, Estevez R (2007) Expression patterns of MLC1 protein in the central and peripheral nervous systems. Neurobiol Dis 26:532-545.

Thrane AS, Thrane VR, Zeppenfeld D, Lou N, Xu Q, Nagelhus Ea, Nedergaard M (2012) General anesthesia selectively disrupts astrocyte calcium signaling in the awake mouse cortex. Proceedings of the National Academy of Sciences 109:18974-18979.

Tobler I, Deboer T, Fischer M (1997) Sleep and sleep regulation in normal and prion protein-deficient mice. The Journal of neuroscience : the official journal of the Society for Neuroscience 17:1869-1879.

Tsujino N, Tsunematsu T, Uchigashima M, Konno K, Yamanaka A, Kobayashi K, Watanabe M, Koyama Y, Sakurai T (2013) Chronic Alterations in Monoaminergic Cells in the Locus Coeruleus in Orexin Neuron-Ablated Narcoleptic Mice. PLoS

1021 ONE 8.
1022 Tsunematsu T, Patel AA, Onken A, Sakata S (2020) State-dependent brainstem
1023 ensemble dynamics and their interactions with hippocampus across sleep states.
1024 Elife 9.
1025 Tsunematsu T, Ueno T, Tabuchi S, Inutsuka A, Tanaka KF, Hasuwa H, Kilduff TS, Terao
1026 A, Yamanaka A (2014) Optogenetic Manipulation of Activity and Temporally
1027 Controlled Cell-Specific Ablation Reveal a Role for MCH Neurons in Sleep/Wake
1028 Regulation. The Journal of neuroscience : the official journal of the Society for
1029 Neuroscience 34:6896-6909.
1030 Tsutsui-Kimura I, Natsubori A, Mori M, Kobayashi K, Drew MR, de Kerchove d'Exaerde
1031 A, Mimura M, Tanaka KF (2017) Distinct Roles of Ventromedial versus
1032 Ventrolateral Striatal Medium Spiny Neurons in Reward-Oriented Behavior. Curr
1033 Biol 27:3042-3048 e3044.
1034 Vyazovskiy VV, Olcese U, Lazimy YM, Faraguna U, Esser SK, Williams JC, Cirelli C,
1035 Tononi G (2009) Cortical Firing and Sleep Homeostasis. Neuron 63:865-878.
1036 Watson BO, Levenstein D, Greene JP, Gelinas JN (2016) Network Homeostasis and
1037 State Dynamics of Neocortical Sleep.1-14.
1038 Weber F, Dan Y (2016) Circuit-based interrogation of sleep control. Nature 538:51-59.
1039 Weber F, Chung S, Beier KT, Xu M, Luo L, Dan Y (2015) Control of REM sleep by
1040 ventral medulla GABAergic neurons. Nature.
1041 Xie L, Kang H, Xu Q, Chen MJ, Liao Y, Thiyagarajan M, O'Donnell J, Christensen DJ,
1042 Nicholson C, Iliff JJ, Takano T, Deane R, Nedergaard M (2013) Sleep drives
1043 metabolite clearance from the adult brain. Science (New York, NY) 342:373-377.
1044 Yoshida K, Tsutsui-Kimura I, Kono A, Yamanaka A, Kobayashi K, Watanabe M, Mimura
1045 M, Tanaka KF (2020) Opposing Ventral Striatal Medium Spiny Neuron Activities
1046 Shaped by Striatal Parvalbumin-Expressing Interneurons during Goal-Directed
1047 Behaviors. Cell Rep 31:107829.
1048 Zeisel A, Hochgerner H, Lonnerberg P, Johnsson A, Memic F, van der Zwan J, Haring M,
1049 Braun E, Borm LE, La Manno G, Codeluppi S, Furlan A, Lee K, Skene N, Harris
1050 KD, Hjerling-Leffler J, Arenas E, Ernfors P, Marklund U, Linnarsson S (2018)
1051 Molecular Architecture of the Mouse Nervous System. Cell 174:999-1014
1052 e1022.

1053

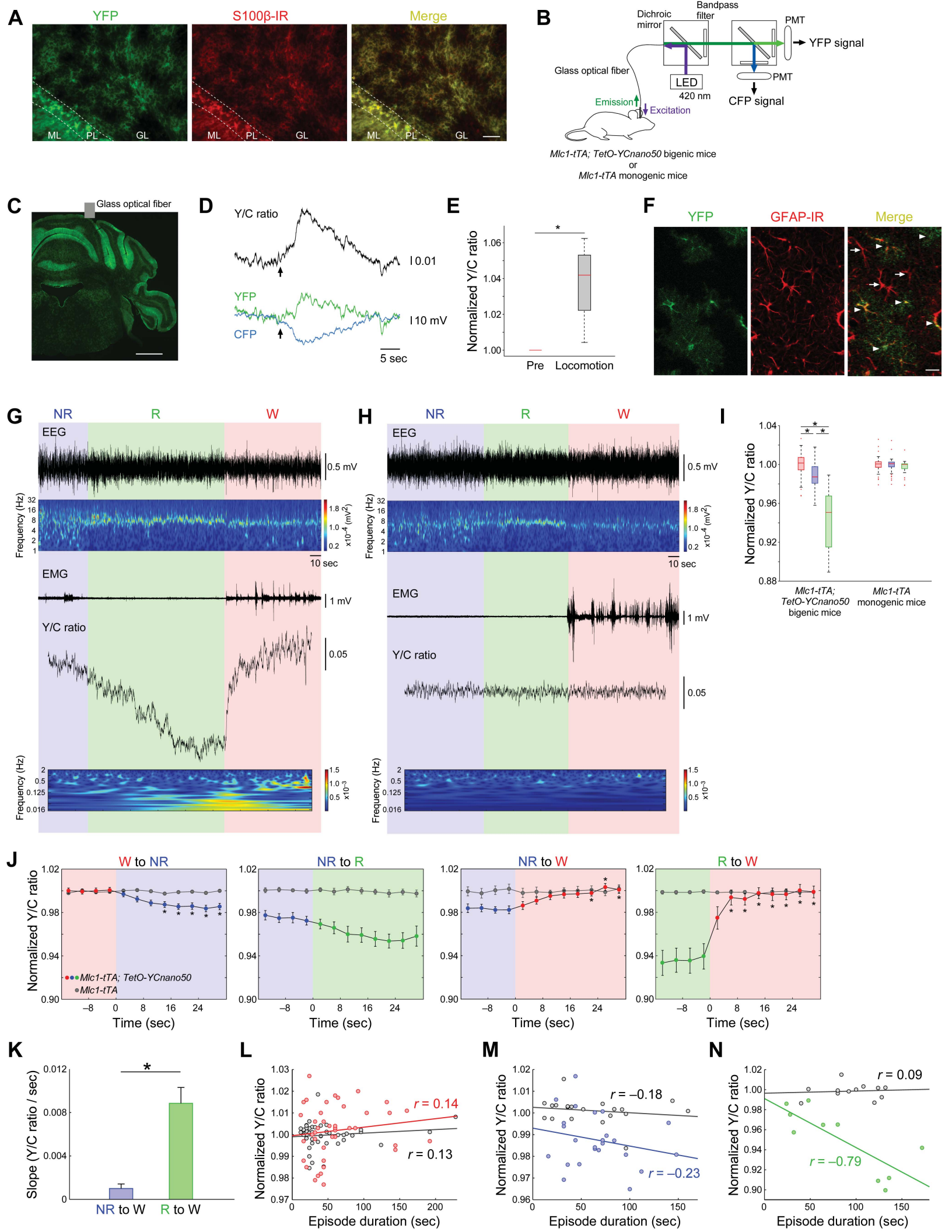
A
YFP
S100β-IR
Merge
ML
PL
GL
B
Dichroic mirror
Bandpass filter
PMT
YFP signal
Glass optical fiber
LED
420 nm
PMT
CFP signal
Emission
Excitation
Mlc1-tTA; TetO-YCnano50 bigenic mice
or
Mlc1-tTA monogenic mice
C
Glass optical fiber
D
Y/C ratio
0.01
YFP
CFP
10 mV
5 sec
E
Normalized Y/C ratio
1.06
1.04
1.02
1.00
*
Pre
Locomotion
F
YFP
GFAP-IR
Merge
G
NR
R
W
EEG
0.5 mV
Frequency (Hz)
32
16
8
4
2
1
1.8
1.0
0.2
x10-4 (mV2)
10 sec
EMG
1 mV
Y/C ratio
0.05
2
0.5
0.125
0.016
1.5
1.0
0.5
x10-3
H
NR
R
W
EEG
0.5 mV
Frequency (Hz)
10 sec
EMG
1 mV
Y/C ratio
0.05
Frequency (Hz)
I
Normalized Y/C ratio
1.04
1.00
0.96
0.92
0.88
*
Mlc1-tTA; TetO-YCnano50 bigenic mice
Mlc1-tTA monogenic mice
J
W to NR
NR to R
NR to W
R to W
Normalized Y/C ratio
1.02
0.98
0.94
0.90
Mlc1-tTA; TetO-YCnano50
Mlc1-tTA
–8
0
8
16
24
Time (sec)
K
Slope (Y/C ratio / sec)
0.012
0.008
0.004
0
*
NR to W
R to W
L
Normalized Y/C ratio
r = 0.14
r = 0.13
Episode duration (sec)
M
Normalized Y/C ratio
r = –0.18
r = –0.23
Episode duration (sec)
N
Normalized Y/C ratio
r = 0.09
r = –0.79
Episode duration (sec)

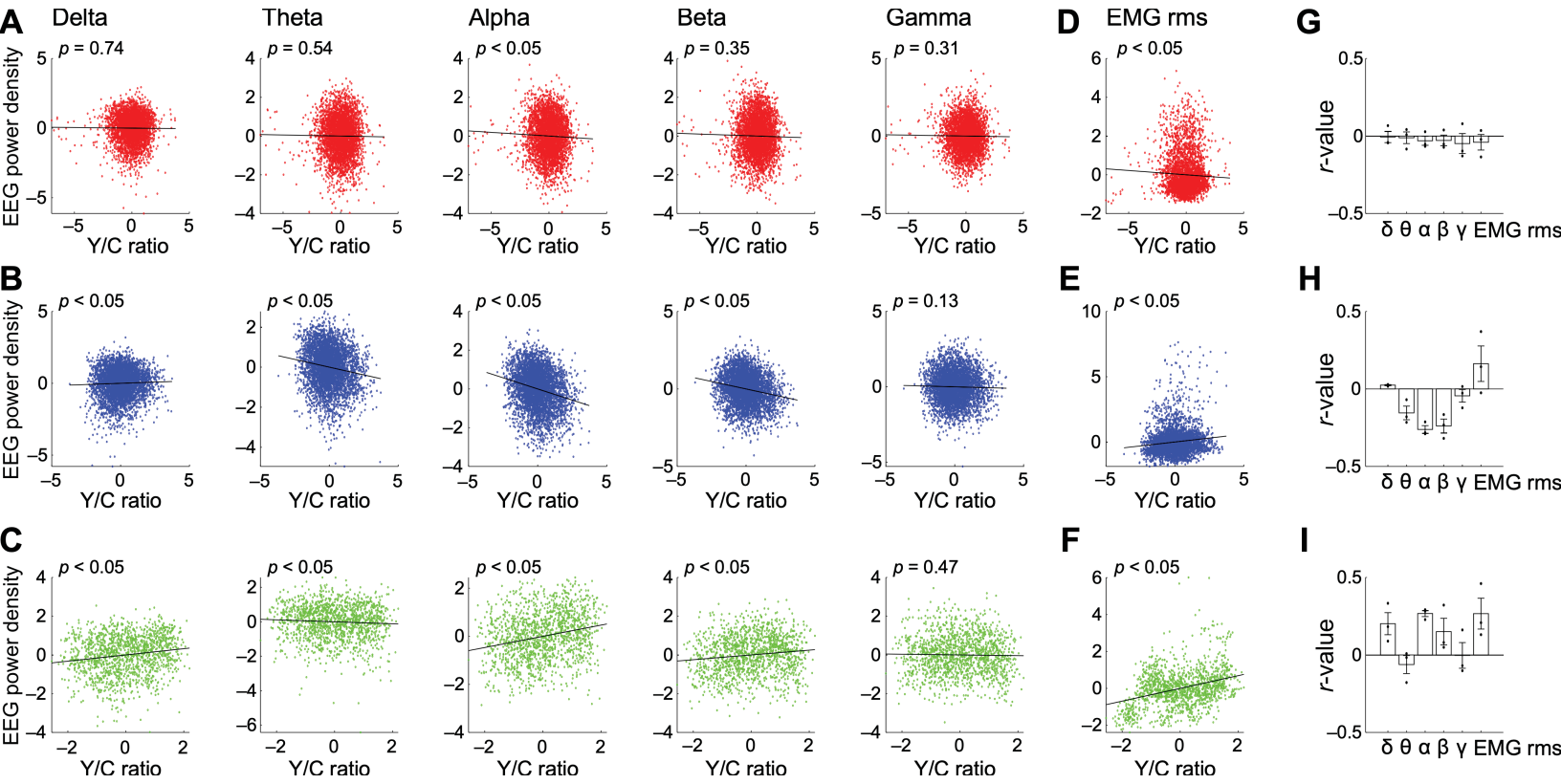
A
Delta
Theta
Alpha
Beta
Gamma
D
EMG rms
G
p = 0.74
p = 0.54
p < 0.05
p = 0.35
p = 0.31
p < 0.05
EEG power density
Y/C ratio
r-value
δ θ α β γ EMG rms
B
E
H
p < 0.05
p < 0.05
p < 0.05
p < 0.05
p = 0.13
p < 0.05
C
F
I
p < 0.05
p < 0.05
p < 0.05
p < 0.05
p = 0.47
p < 0.05

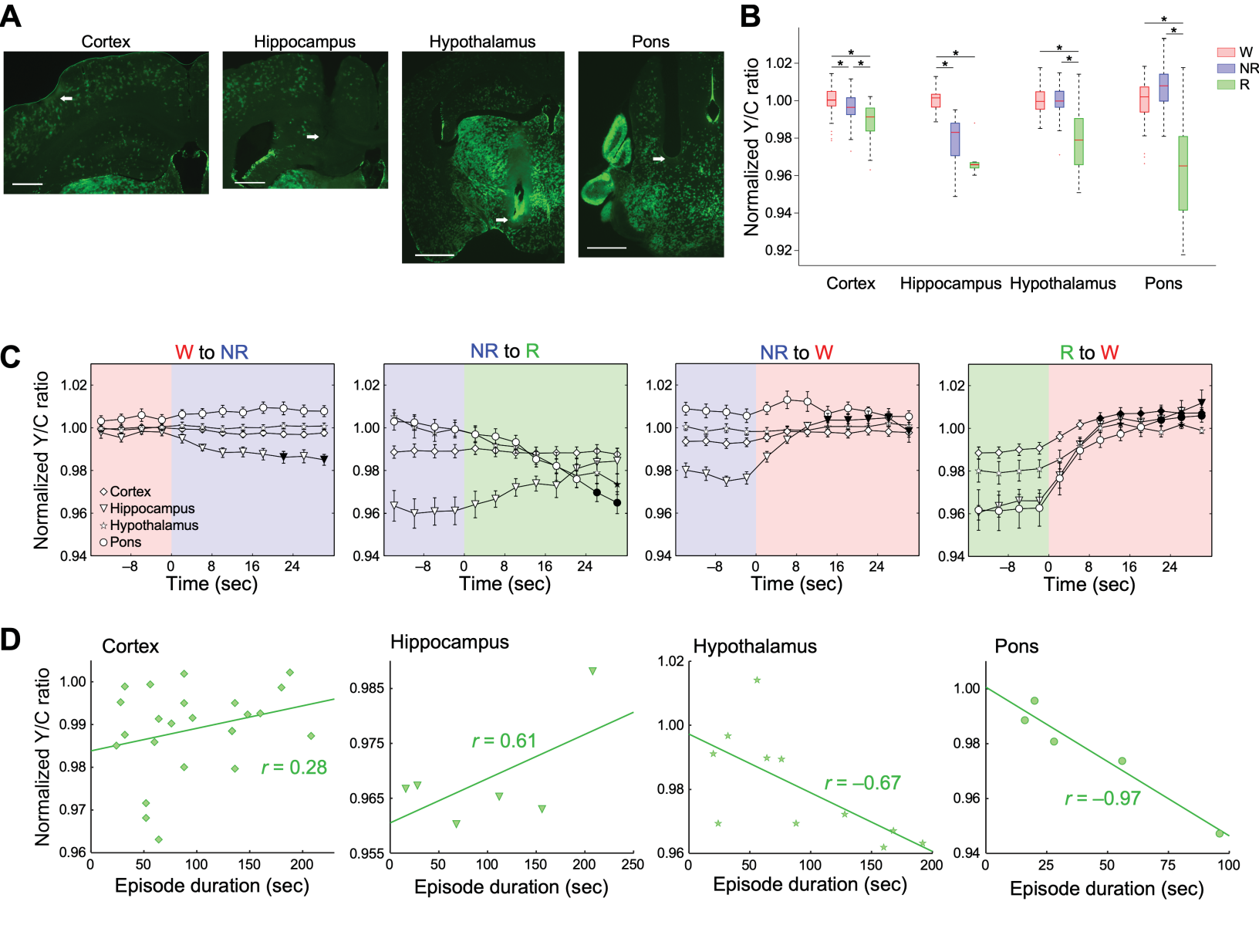
A
Cortex
Hippocampus
Hypothalamus
Pons
B
Normalized Y/C ratio
1.02
1.00
0.98
0.96
0.94
0.92
Cortex
Hippocampus
Hypothalamus
Pons
W
NR
R
C
W to NR
NR to R
NR to W
R to W
Normalized Y/C ratio
Cortex
Hippocampus
Hypothalamus
Pons
–8
0
8
16
24
Time (sec)
D
Cortex
Hippocampus
Hypothalamus
Pons
Normalized Y/C ratio
r = 0.28
r = 0.61
r = –0.67
r = –0.97
Episode duration (sec)

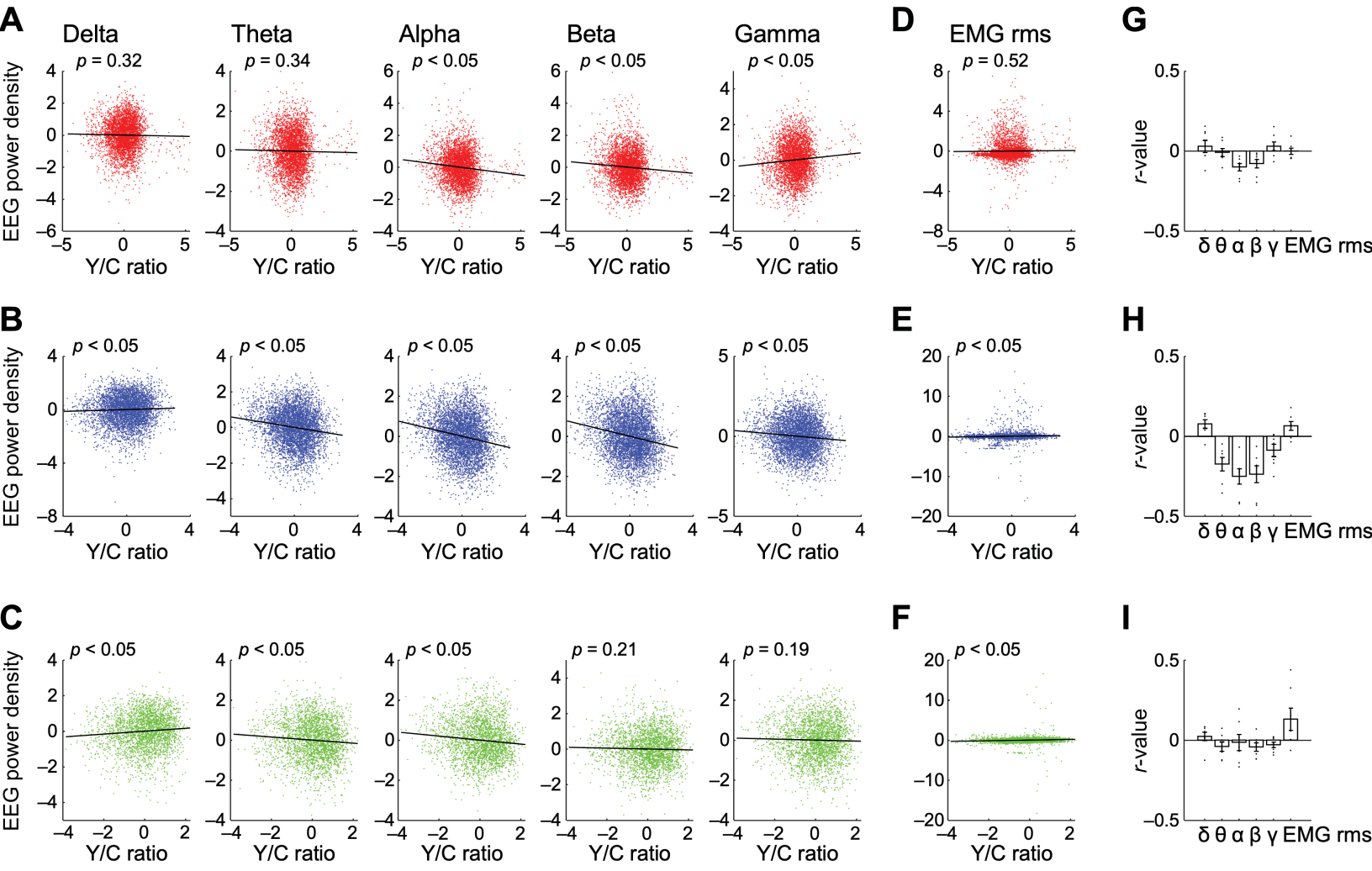
A
Delta
Theta
Alpha
Beta
Gamma
p = 0.32
p = 0.34
p < 0.05
p < 0.05
p < 0.05
EEG power density
Y/C ratio
D
EMG rms
p = 0.52
G
r-value
δ θ α β γ EMG rms
B
p < 0.05
E
H
C
p < 0.05
p = 0.21
p = 0.19
F
I

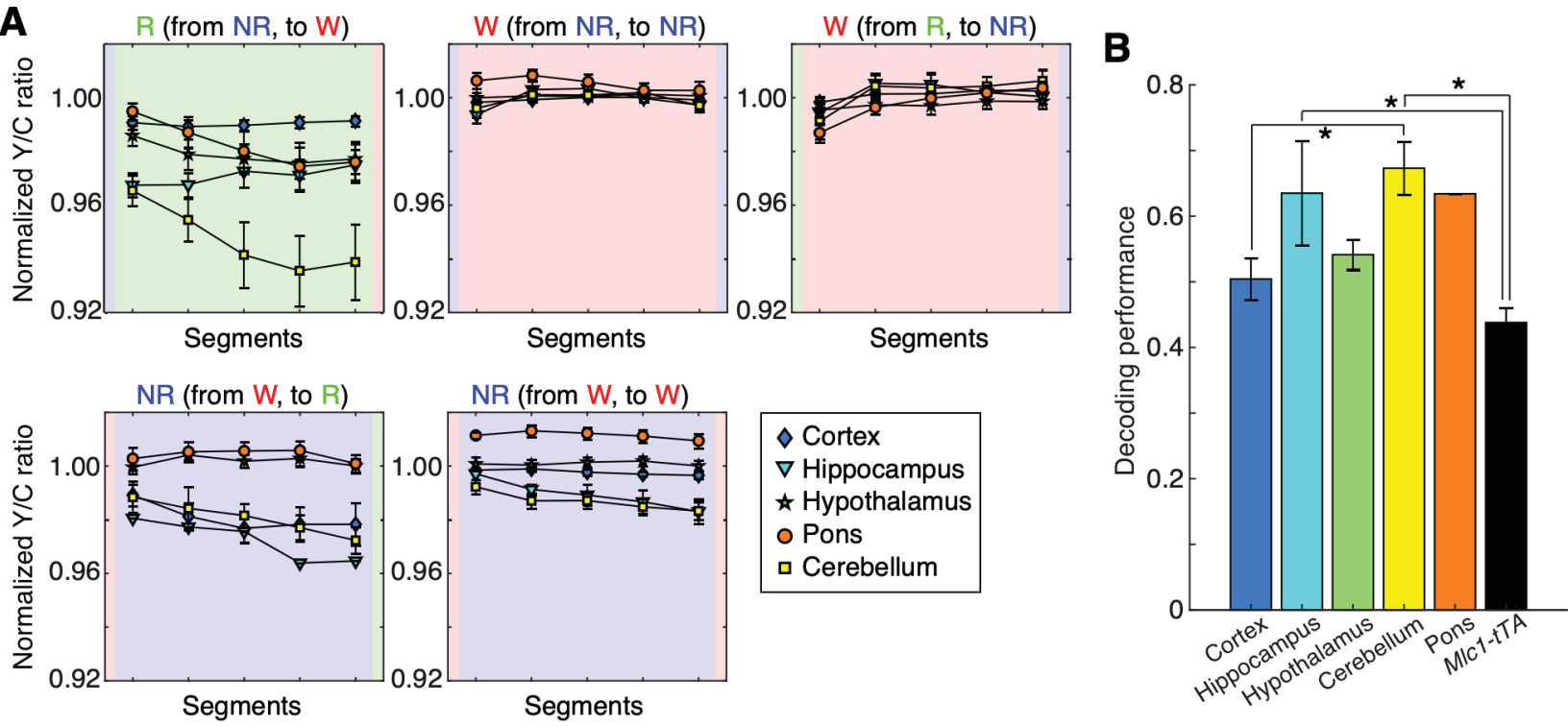
A
R (from NR, to W)
W (from NR, to NR)
W (from R, to NR)
NR (from W, to R)
NR (from W, to W)
Normalized Y/C ratio
1.00
0.96
0.92
Segments
Cortex
Hippocampus
Hypothalamus
Pons
Cerebellum
B
Decoding performance
0.8
0.6
0.4
0.2
0
*
Cortex
Hippocampus
Hypothalamus
Cerebellum
Pons
Mlc1-tTA

Table 1. Sleep architecture in mice in the head-fixed condition and freely moving condition

	Wakefulness	NREM	REM
Episode duration (sec)			
Free-moving condition of *Mlc1*-tTA mice	158.7 ± 25.5	187.3 ± 14.9	87.8 ± 14.5
Free-moving condition of *Mlc1*-tTA; TetO-YCnano50 mice	197.0 ± 24.6	205.8 ± 18.7	62.3 ± 6.0
Head-fixed condition without recording from hypothalamus of *Mlc1*-tTA; TetO-YCnano50 mice	134.6 ± 32.7	105.7 ± 18.4*	90.9 ± 7.5
Head-fixed condition with recording from hypothalamus of *Mlc1*-tTA; TetO-YCnano50 mice	102.1 ± 36.9	106.3 ± 13.8	86.8 ± 26.4
Time spent in each state (%)			
Freely moving condition of *Mlc1*-tTA mice	42.6 ± 4.9	52.2 ± 3.4	5.2 ± 1.1
Freely moving condition of *Mlc1*-tTA; TetO-YCnano50 mice	46.6 ± 3.1	49.5 ± 2.7	3.9 ± 0.9
Head-fixed condition without recording from hypothalamus	48.4 ± 6.2	43.4 ± 5.1	8.2 ± 1.5
Head-fixed condition with recording from hypothalamus	41.9 ± 7.4	51.6 ± 5.2	6.5 ± 3.4

Data are shown as means ± SD.

*$p < 0.05$, head-fixed condition without recording from hypothalamus vs freely moving condition of *Mlc1*-tTA mice and freely moving condition of *Mlc1*-tTA; TetO-YCnano50 mice

Table 2. Summary of region-specific and state-dependent astrocyte Ca^{2+} dynamics in mice

		Cortex	Hippocampus	Hypothalamus	Pons	Cerebellum
Normalized Y/C ratio	NR (vs W)	↓	↓	→	→	↓
	R (vs W)	↓	↓	↓	↓	↓
	R (vs NR)	↓	→	↓	↓	↓
State transition	W to NR	→	↓	→	→	↓
	NR to R	→	→	↓	↓	→
	NR to W	→	↑	→	→	↑
	R to W	↑	↑	↑	↑	↑
In episode	R (from NR, to W)	→	→	↓	↓	↓
	NR (from W, to R)	↓	↓	→	→	↓
Episode duration	R	→	→	↓	↓	↓

NR, NREM sleep; R, REM sleep; W, wakefulness.